ELSEVIER

# Modeling NCA/C$_6$-Si battery ageing

Zhiqiang Chen [a,b], Dmitri L. Danilov [a,b], Qian Zhang [b,c], Ming Jiang [a,b], Jiang Zhou [d], Rüdiger-A. Eichel [b,c], Peter H.L. Notten [a,b,e,*]

[a] Eindhoven University of Technology, Eindhoven 5600, MB, the Netherlands
[b] Fundamental Electrochemistry (IEK-9), Forschungszentrum Jülich, D-52425, Germany
[c] RWTH Aachen University, Aachen D-52074, Germany
[d] Tianjin Institute of Power Sources, Tianjin 300384, China
[e] University of Technology Sydney, Broadway, Sydney, NSW 2007, Australia

## ARTICLE INFO

## ABSTRACT

The rapidly growing demand for energy storage has spurred the development of advanced Li-ion batteries. Physical-based modeling techniques have emerged as a powerful tool to assist the development of battery technologies because of the advantages of relating battery performances to internal physical and (electro) chemical processes. In the present paper, a pseudo-two-dimensional (P2D) based model has been developed for Li-ion batteries with NCA cathodes and C$_6$/Si blended anodes. Coupled with a solid electrolyte interface (SEI) growth model and a loss of active materials (LAM) model, the P2D-based model has been applied to simulate the electrochemical behavior of pristine cells and the degradation of aged cells. For pristine cells, a competing reaction occurs between C$_6$ and Si during (dis)charge, resulting in a sequential (de)lithiation and diverse stress behavior. For aged cells, the SEI growth mainly causes the battery capacity to fade under different cycling conditions. LAM also plays an important role in battery capacity loss. SEI growth is sensitive to the temperature, cycle time, cycle number, and cycle current, while LAM is significantly influenced by temperature and current. During storage, the main factor causing battery capacity losses is the SEI growth, which is affected by the storage time, storage state-of-charge, and temperature.

## 1. Introduction

In recent years, lithium-ion batteries (LIB) have become the fundamental components for portable electronic devices and electric vehicles because of their advantages, such as high energy/power density, long cycle life, and low cost [1]. Various efforts have been made with the increasing demand for high energy/power LIB [1–3]. From the material level, high specific energy active materials have been considered extensively.

Layered nickel-rich material, LiNi$_{0.8}$Co$_{0.15}$Al$_{0.05}$O$_2$ (NCA), is an attractive cathode material and has multiple advantages, *i.e.* high gravimetric and volumetric energy density, high power density, and long cycle life [2,3]. The low cobalt and high nickel content also make this cathode material environmentally friendly, inexpensive, and thermally stable. Owing to these merits, NCA has been commercially adopted for high energy/power LIB [4,5].

Graphite (C$_6$) is a conventional anode active material with good Li (de)intercalation reversibility and long cycle life [6,7]. Still, it has a

relatively low theoretical capacity (372 mAh g$^{-1}$ for LiC$_6$) [6]. Silicon (Si) is a promising anode material due to its large theoretical capacity of 3579 mAh g$^{-1}$ (corresponding to Li$_{15}$Si$_4$) and favorable (de)lithiation potential (*vs.* Li$^+$/Li) [8,9]. However, some critical disadvantages of Si severely restrain its applications, such as the large particle volume change and particle crack/pulverization [8–10]. Therefore, the combination of C$_6$ and Si has been proposed as a blended anode to achieve both a high capacity and long cycle life [11–14]. Some commercial applications have been reported [14–18]. In the present paper, a battery system combining an NCA cathode and a C$_6$/Si blended anode is selected to investigate the aging of high-energy/power LIB.

Degradation is an unpleasant and unavoidable issue that happens in all LIB systems and leads to battery capacity/power fade [19]. Various degradation mechanisms have been proposed and validated [20], including solid electrolyte interface (SEI) formation and growth, Li plating, active particle structural disordering, loss of active materials (LAM), *etc.* Among all the degradation mechanisms, SEI growth is recognized as the dominant mechanism in most operating scenarios [21, 22]. SEI is an electronically insulating and ionically conducting

---

## Nomenclature

*P2D based model*

| | |
|---|---|
| $a_m$ | Specific interfacial area of the porous electrode, $m =$ C, Si, $p$ ($\text{m}^{-1}$) |
| $brugg_m$ | Bruggeman coefficient in the porous electrode and separator membrane region, $m = n, sep, p$ (-) |
| $c_{1,m}$ | Li concentration in the solid particle, $m =$ C, Si, $p$ ($\text{mol m}^{-3}$) |
| $c_{1,m}^s$ | Surface Li concentration of the solid particle, $m =$ C, Si, $p$ ($\text{mol m}^{-3}$) |
| $c_{1,m}^0$ | Initial Li concentration of the solid particle, $m =$ C, Si, $p$ ($\text{mol m}^{-3}$) |
| $\bar{c}_{1,m}$ | The difference of Li-concentration with the reference concentration, *i.e.* $\bar{c}_{1,m} = c_{1,m} - c_{1,m}^0$, $m =$ C, Si ($\text{mol m}^{-3}$) |
| $c_2$ | Li concentration in the electrolyte ($\text{mol m}^{-3}$) |
| $D_2$ | Salt diffusion coefficient in the electrolyte ($\text{m}^2\,\text{s}^{-1}$) |
| $D_{2,m}^{eff}$ | Effective salt diffusion coefficient in the electrolyte at the porous electrode and separator regions $D_{2,i}^{eff} = D_{2,i}(\varepsilon_i)^{brugg_i}$, $m = n, sep, p$ ($\text{m}^2\,\text{s}^{-1}$) |
| $D_{1,m}$ | Li diffusion coefficient in the solid particle, $m =$ C, Si, $p$ ($\text{m}^2\,\text{s}^{-1}$) |
| $F$ | Faraday's constant, 96487 ($\text{C mol}^{-1}$) |
| $i_1$ | Current density in the solid ($\text{A m}^{-2}$) |
| $i_2$ | Current density in the electrolyte ($\text{A m}^{-2}$) |
| $I$ | Applied current density ($\text{A m}^{-2}$) |
| $i_m^0$ | Exchange current density of charge-transfer reactions, $m =$ C, Si, $p$ ($\text{A m}^{-2}$) |
| $j_m$ | Reaction-rate distribution inside the porous electrode, $m =$ C, Si, $p$ ($\text{mol m}^{-2}\,\text{s}^{-1}$) |
| $k_m$ | Kinetic constant of the porous electrode, $m =$ C, Si, $p$ ($\text{m}^{2.5}\,\text{mol}^{-0.5}\,\text{s}^{-1}$) |
| $L$ | Thickness of the cell, equal to $\delta_n + \delta_{sep} + \delta_p$ (m) |
| $r_m$ | Radius vector of the active materials particle, $m =$ C, Si, $p$ (-) |
| $R$ | Gas constant, 8.314 ($\text{J mol}^{-1}\,\text{K}^{-1}$) |
| $R_f$ | Current collector ohmic resistance and other electrical conducting resistance ($\Omega\text{m}^2$) |
| $R_{film,m}$ | SEI film resistance $m =$ C, Si ($\Omega\text{m}^2$) |
| $R_m$ | Radius of the solid particle, $m =$ C, Si, $p$ (m) |
| $t$ | Time vector (s) |
| $t_+$ | Transference number of Li-ions in the electrolyte (-) |
| $T$ | Temperature (K) |
| $U_m$ | Equilibrium potential of active materials in porous electrodes, $m =$ C, Si, $p$ (V) |
| $U_m^s$ | Surface potential of active materials, $m =$ C, Si, $p$ (V) |
| $x$ | Normalized position vector along the thickness direction of the battery (-) |
| $\alpha_m$ | Anodic charge-transfer coefficient, $m =$ C, Si, $p$ (-) |
| $\delta_m$ | Thickness of porous electrodes and separator, $m = n, sep, p$ (m) |
| $\varepsilon_m$ | Porosity of porous electrodes and separator, $m = n, sep, p$ (-) |
| $\eta_m^{ct}$ | Charge-transfer overpotential inside the porous electrode, $m =$ C, Si, $p$ (V) |
| $\Phi_1$ | Electric potential in the solid (V) |
| $\Phi_2$ | Electric potential in the electrolyte (V) |
| $\kappa_m$ | Ionic conductivity in the electrolyte, $m = n, sep, p$ (S m$^{-1}$) |
| $\sigma_m$ | Electronic conductivity in the solid, $m = n, p$ (S m$^{-1}$) |
| $\kappa_m^{eff}$ | Effective ionic conductivity in the electrolyte at the porous electrode and separator region $\kappa_m^{eff} = \kappa_m(\varepsilon_m)^{brugg_m}$, $m = n, sep, p$ (S m$^{-1}$) |
| $\sigma_m^{eff}$ | Effective electronic conductivity of the porous electrode $\sigma_m^{eff} = \sigma_m(1 - \varepsilon_m)$, (S m$^{-1}$) |
| $f_\pm$ | Activity coefficient of electrolyte salt, (-) |
| $E_m$ | Young's modulus, $m =$ C, Si (Pa) |
| $\sigma_{r,m}$ | Radial stress, $m =$ C, Si (Pa) |
| $\sigma_{\theta,m}$ | Tangential stress, $m =$ C, Si (Pa) |
| $\sigma_{h,m}$ | Hydrostatic stress, $m =$ C, Si (Pa) |
| $\varepsilon_{r,m}$ | Radial strain, $m =$ C, Si (-) |
| $\varepsilon_{\theta,m}$ | Tangential strain, $m =$ C, Si (-) |
| $u_m$ | Displacement, $m =$ C, Si (m) |
| $\upsilon_m$ | Poisson's ratio, $m =$ C, Si (-) |
| $\Omega_m$ | Partial molar volume, $m =$ C, Si ($\text{m}^3\,\text{mol}^{-1}$) |

*Subscripts*

| | |
|---|---|
| 1 | Properties in the solid phase of the electrode |
| 2 | Properties in the electrolyte phase |
| n | Negative porous electrode |
| sep | Porous separator |
| p | Positive porous electrode |

*Superscripts*

| | |
|---|---|
| s | Surface |
| ct | Charge-transfer |
| eff | Effective properties |

*Aging model*

| | |
|---|---|
| $\Delta E_m$ | Energy barrier, $m =$ C, Si (eV) |
| $j_{SEI,m}$ | Reaction rate of the SEI formation, $m =$ C, Si ($\text{mol m}^{-2}\,\text{s}^{-1}$) |
| $j_{tl,m}$ | Electron tunneling induced reaction rate, $m =$ C, Si ($\text{mol m}^{-2}\,\text{s}^{-1}$) |
| $j_{tot}$ | Total reaction rate ($\text{mol m}^{-2}\,\text{s}^{-1}$) |
| $k_{LAM,m}$ | The rate of loss of active material, $m =$ C, Si ($\text{A}^{-1}\,\text{s}^{-1}$) |
| $l_{tot,m}^{in}$ | Total inner SEI layer thickness, $m =$ C, Si (m) |
| $l_{0,m}^{in}$ | Initial inner SEI layer thickness, $m =$ C, Si (m) |
| $l_{inc,m}^{in}$ | Increased inner SEI layer thickness during aging, $m =$ C, Si (m) |
| $l_{tot,m}^{out}$ | Total outer SEI layer thickness, $m =$ C, Si (m) |
| $l_{SEI,m}$ | Total SEI thickness including inner and outer SEI layer, $m =$ C, Si (m) |
| $m_e$ | Electron mass (kg) |
| $M_m$ | Molar mass, $m =$ SEI, Li, C (g mol$^{-1}$) |
| $N_{SEI,m}^{Li}$ | Loss of Li due to the SEI formation at the surface of $m$ particle, $m =$ C, Si ($\text{mol m}^{-3}$) |
| $P_0$ | Electron tunneling probability (-) |
| $Q_{SEI,m}^{Li}$ | Capacity loss caused by active Li immobilization in the SEI, $m =$ C, Si (Ah) |
| $Q_{LAM,m}$ | Capacity loss caused by loss of active materials, $m =$ C, Si (Ah) |
| SoC | State of charge, (-) |
| $V$ | Volume of the porous electrode ($\text{m}^3$) |
| $\delta_m^{in}$ | Percentage of inner SEI thickness on the total SEI thickness, $m =$ C, Si |
| $\kappa_{SEI,m}$ | Conductivity of the SEI, $m =$ C, Si (S m$^{-1}$) |
| $\rho_m$ | Density, $m =$ SEI, Li, C (g mol$^{-1}$) |
| $\nu_e$ | Fermi velocity of electron in the bulk of active materials (m s$^{-1}$) |
| $\hbar$ | Reduced Planck constant ($1.055 \times 10^{-34}$ J s) |

passivation film formed at the surface of anode active materials, such as $C_6$, Si, and alkali metals. It grows extremely fast at the first charging (formation) process [23,24]. Once a stable SEI has been formed, it will protect the electrode active materials from further severe corrosion and deterioration. The structure of SEI is complex. A compact and inorganic inner layer is attached closely to the surface of the active material, also called inner SEI. Inner SEI permits Li-ions transport but prohibits solvent molecules. A porous, mostly organic layer is formed between the inner SEI and bulk electrolyte, called the outer SEI. It allows the transport of both Li-ions and electrolyte solvent [25,26]. The thickness of the inner SEI is in the several nanometers range, and the outer SEI is ranged from tens to hundreds of nanometers [26]. The continuous growth of SEI causes irreversible $Li^+$ consumption, which finally leads to battery irreversible capacity losses.

LAM also causes irreversible battery capacity and power losses [20, 27]. LAM can be further explained due to active particle cracking, loss of electrical contact, active site blocking, *etc*. During the (de)intercalation, the Li concentration gradient is built inside active material particles because of the transport limitations, further causing strain and stress. This kind of stress, generated at the particle level, is called diffusion-induced stress (DIS) [28]. DIS provides a significant driving force for particle crack, breakage, and isolation [29,30]. DIS is influenced by material properties, *i.e.* diffusion coefficient, mechanical properties, volume changes, *etc*. In addition, other factors, such as the formation of inactive layers at the surface of active particles [31], metal dissolution and precipitation [32], phase change, and oxygen evolution [33], can also incur active material losses.

Numerical modeling is a helpful tool in investigating the electrochemical and aging behavior of LIB. The physical-based pseudo-two-dimensional (P2D) model, using a combination of the porous electrode theory and concentrated solution theory [34–38], provides a basic theoretical framework for the physical and electrochemical processes taking place inside LIB. Integrating aging models into the physical-based P2D model is popular to simultaneously simulate the electrochemical and aging behaviors of LIB [21,30,39–41]. The most adopted SEI growth model uses a cathodic Butler-Volmer type equation [21], in which the solvent concentration and the overpotential significantly influence the formation rate. Another approach to describe the SEI growth is related to the electron tunneling process, in which electrons crossing over the electrically insulated inner SEI is considered the rate-determining step. For example, Li *et al.* [26,42] analytically derived a closed-form expression for SEI formation by solving the quantum-mechanical electron tunneling problem, and the capacity loss was also analytically derived. The resulted capacity loss model was successfully applied to predict the cycle life of different types of batteries [26, 43-45].

Different approaches have been proposed to model LAM. Since DIS provides the driving force for particle cracking and breakage, various criteria for LAM have been used based on DIS. Reniers *et al.* [27] suggested using the ratio of maximum hydrostatic stress and the yield stress as the indicator for LAM, and some related parameters needed to be fit. Cheng *et al.* [46] indicated the total strain energy stored in the particles provided the driving force for fracturing and can be obtained by integrating the strain energy over the entire volume of the spherical particle during operation. Yang *et al.* [39] and Liang *et al.* [40] used a critical limit value of total strain energy to indicate LAM. Due to the periodical volume changes and DIS during cycling, Jin *et al.* [47,48] related LAM directly to the applied current. The rate of LAM is a function of current, working time, temperature, the activation energy. Good fits can also be found under various cycling conditions.

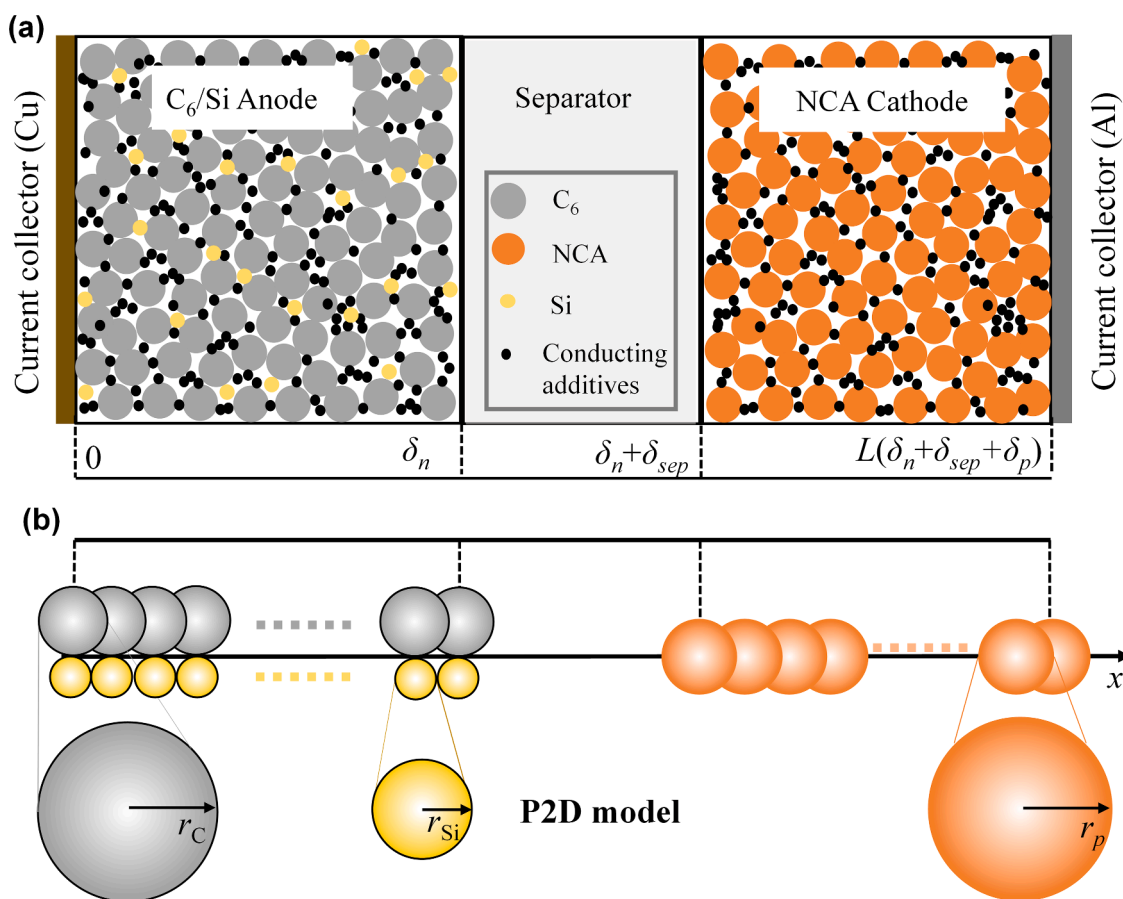In the present paper, a high energy/power battery system with NCA



**Fig. 1.** (a) Schematic illustration of a typical Li-ion battery consisting of a porous anode, a porous cathode, and a porous separator. The anode active materials are $C_6$ and Si particles, and the active material in the cathode is NCA particles. (b) The configuration of the P2D model based on the components of this cell.

cathode and $C_6$/Si blended anode is selected as the research subject. The corresponding P2D model with blended anode implemented was built. The electrochemical behavior of pristine cells was simulated with this P2D model. Subsequently, an electron-tunneling-based SEI growth model and LAM model were integrated into the P2D model. With this model, cycling-induced and storage-induced aging were systematically investigated under various operating conditions.
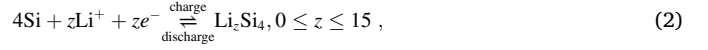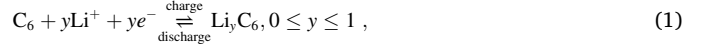
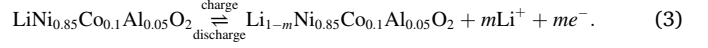## 2. Model development

### 2.1. Pristine cells

#### 2.1.1. P2D model

Fig. 1a presents the schematic representation of a Li-ion cell with a porous anode, a porous cathode, and a porous separator. The pores in all porous structures are filled with liquid electrolyte. In this cell, the active materials in the anode are a blend of $C_6$ and Si. The cathode active materials are NCA. $\delta_n$, $\delta_{sep}$ and $\delta_p$ represent the thickness of the anode, separator, and cathode, respectively. The total thickness is denoted as $L$. The electrochemical reactions taking place inside this battery during

(dis)charging can be represented as

$$C_6 + yLi^+ + ye^- \underset{\text{discharge}}{\overset{\text{charge}}{\rightleftharpoons}} Li_y C_6, 0 \le y \le 1 , \tag{1}$$

$$4Si + zLi^+ + ze^- \underset{\text{discharge}}{\overset{\text{charge}}{\rightleftharpoons}} Li_z Si_4, 0 \le z \le 15 , \tag{2}$$

and

$$LiNi_{0.85}Co_{0.1}Al_{0.05}O_2 \underset{\text{discharge}}{\overset{\text{charge}}{\rightleftharpoons}} Li_{1-m}Ni_{0.85}Co_{0.1}Al_{0.05}O_2 + mLi^+ + me^- . \tag{3}$$

Eqs. (1) and (2) give the charge-transfer reactions at the anode, and Eq. (3) shows the reaction at the cathode. $y$, $z$, and $m$ represent the normalized charge-transfer numbers at $C_6$, Si, and NCA. Note that a competing charge-transfer reaction happens between $C_6$ and Si during (dis)charge. Fig. 1b shows the corresponding configuration of the P2D model based on the components of this cell, including a series of solid particles lining up in the $x$ direction. On the anode side, $C_6$ and Si particles are assumed to locate at the same discrete position and to contact each other. $r_C$, $r_{Si}$, and $r_p$ are the space vectors inside $C_6$, Si, and NCA

**Table 1**
Governing equations in a P2D model for an NCA/$C_6$-Si cell.

| | Governing equations | Eq. | Boundary and initial conditions |
|---|---|---|---|
| **Anode region** $0 \le x \le \delta_n$, ($n$=negative electrode (anode), $m$ = C, Si) | | | |
| Diffusion in particles | $\frac{\partial c_{1,m}}{\partial t} = \frac{1}{r_m^2}\frac{\partial}{\partial r_m}\left(r_m^2 D_{1,m}\frac{\partial c_{1,m}}{\partial r_m}\right)$ | 4 | $-D_{1,m}\frac{\partial c_{1,m}}{\partial r_m}\big|_{r=R_i} = j_m, \frac{\partial c_{1,m}}{\partial r_m}\big|_{r_m=0} = 0,$ $c_{1,m}\big|_{t=0} = c_{1,m}^0$ |
| Kinetics | $j_m = \frac{i_m^0}{F}\left[\exp\left(\frac{\alpha_m F \eta_m^{ct}}{RT}\right) - \exp\left(-\frac{(1-\alpha_m)F\eta_m^{ct}}{RT}\right)\right]$ | 5 | - |
| | $\eta_m^{ct} = \Phi_1 - \Phi_2 - R_{film,m}Fj_m - U_m^s$ | 6 | - |
| | $i_m^0 = Fk_m(c_{1,m}^{max} - c_{1,m}^s)^{\alpha_m}(c_{1,m}^s)^{1-\alpha_m}(c_2)^{\alpha_m}$ | 7 | - |
| Mass balance | $\varepsilon_n\frac{\partial c_2}{\partial t} = \frac{\partial}{\partial x}\left(D_{2,n}^{eff}\frac{\partial c_2}{\partial x}\right) + \sum a_m j_m(1-t_+)$ | 8 | $D_{2,n}^{eff}\frac{\partial c_2}{\partial x}\big|_{x=0} = 0,$ $D_{2,n}^{eff}\frac{\partial c_2}{\partial x}\big|_{x=\delta_n} = D_{2,sep}^{eff}\frac{\partial c_2}{\partial x}\big|_{x=\delta_n}$ |
| Potential in solution | $i_2 = -\kappa_n^{eff}\frac{\partial \Phi_2}{\partial x} + \frac{2\kappa_n^{eff}RT}{F}(1-t_+)\left(1+\frac{d\ln f_\pm}{d\ln c_2}\right)\frac{\partial \ln c_2}{\partial x}$ | 9 | $i_2\big|_{x=0} = 0, i_2\big|_{x=\delta_n} = I$ |
| Potential in solid | $i_1 = -\sigma_n^{eff}\frac{\partial \Phi_1}{\partial x}$ | 10 | $i_1\big|_{x=0} = I, i_1\big|_{x=\delta_n} = 0,$ $i_1\big|_{x=\delta_n+\delta_{sep}} = 0, i_1\big|_{x=L} = I$ |
| | $i_1 + i_2 = I$ | 11 | - |
| | $\sum a_m j_m = \frac{1}{F}\frac{\partial i_2}{\partial x}$ | 12 | - |
| **Separator region** $\delta_n \le x \le \delta_n + \delta_{sep}$ | | | |
| Mass balance | $\varepsilon_{sep}\frac{\partial c_2}{\partial t} = \frac{\partial}{\partial x}\left(D_{2,sep}^{eff}\frac{\partial c_2}{\partial x}\right)$ | 13 | See Eqs. (8) and (19) |
| Potential in solution | $i_2 = -\kappa_{sep}^{eff}\frac{\partial \Phi_2}{\partial x} + \frac{2\kappa_{sep}^{eff}RT}{F}(1-t_+)\left(1+\frac{d\ln f_\pm}{d\ln c_2}\right)\frac{\partial \ln c_2}{\partial x}$ | 14 | $i_2 = I$ |
| **Cathode region** $\delta_n + \delta_{sep} \le x \le L$, ($p$=positive electrode (cathode)) | | | |
| Diffusion in particles | $\frac{\partial c_{1,p}}{\partial t} = \frac{1}{r_p^2}\frac{\partial}{\partial r_p}\left(r_p^2 D_{1,p}\frac{\partial c_{1,p}}{\partial r_p}\right)$ | 15 | $-D_{1,p}\frac{\partial c_{1,p}}{\partial r_p}\big|_{r=R_p} = j_p, \frac{\partial c_{1,p}}{\partial r_p}\big|_{r_p=0} = 0$ $c_{1,p}\big|_{t=0} = c_{1,p}^0$ |
| Kinetics | $j_p = \frac{i_p^0}{F}\left[\exp\left(\frac{\alpha_p F \eta_p^{ct}}{RT}\right) - \exp\left(-\frac{(1-\alpha_p)F\eta_p^{ct}}{RT}\right)\right]$ | 16 | - |
| | $\eta_p^{ct} = \Phi_1 - \Phi_2 - U_p^s$ | 17 | - |
| | $i_p^0 = Fk_p(c_{1,p}^{max} - c_{1,p}^s)^{\alpha_p}(c_{1,p}^s)^{1-\alpha_p}(c_2)^{\alpha_p}$ | 18 | - |
| Mass balance | $\varepsilon_p\frac{\partial c_2}{\partial t} = \frac{\partial}{\partial x}\left(D_{2,p}^{eff}\frac{\partial c_2}{\partial x}\right) + a_p j_p(1-t_+)$ | 19 | $D_{2,p}^{eff}\frac{\partial c_2}{\partial x}\big|_{x=\delta_n+\delta_{sep}} = D_{2,sep}^{eff}\frac{\partial c_2}{\partial x}\big|_{x=\delta_n+\delta_{sep}},$ $D_{2,p}^{eff}\frac{\partial c_2}{\partial x}\big|_{x=L} = 0$ |
| Potential in solution | $i_2 = -\kappa_p^{eff}\frac{\partial \Phi_2}{\partial x} + \frac{2\kappa_p^{eff}RT}{F}(1-t_+)\left(1+\frac{d\ln f_\pm}{d\ln c_2}\right)\frac{\partial \ln c_2}{\partial x}$ | 20 | $i_2\big|_{x=\delta_n+\delta_{sep}} = I,$ $i_2\big|_{x=L} = 0$ |
| Potential in solid | $i_1 = -\sigma_p^{eff}\frac{\partial \Phi_1}{\partial x}$ | 21 | $i_1\big|_{x=\delta_n+\delta_{sep}} = 0,$ $i_1\big|_{x=L} = I$ |
| | $i_1 + i_2 = I$ | 22 | - |
| | $a_p j_p = \frac{1}{F}\frac{\partial i_2}{\partial x}$ | 23 | - |
| **Battery output voltage** | | | |
| | $V_{bat} = \Phi_1\big|_{x=L} - \Phi_1\big|_{x=0} - IR_f$ | 24 | - |

particles. Note that the subscript C denotes $C_6$ for simplicity.

The P2D model is adopted to describe the various physical and electrochemical processes occurring in NCA/$C_6$-Si batteries. The governing equations are summarized in Table 1, where parameter definitions are listed in the nomenclature. These equations include the mass balance in the electrolyte at the anode, separator, and cathode regions (Eqs. (8), (13), and (19)), the electric potential distribution in the solid phase at the anode and cathode region (Eqs. (10) and (21)), the electric potential distribution in solution phase at the anode, separator, and cathode region (Eqs. (9), (14) and (20)), the charge balance in anode and cathode (Eqs. (11), (12), (22) and (23)), the charge-transfer kinetics for anode and cathode (Eqs. (5)-(7) and (16)-(18)), and diffusion in the spherical particles for anode and cathode (Eq. (4) and (15)). The battery output voltage is given by Eq. (24). It is worth mentioning that kinetic and diffusion in particles need to be considered separately for $C_6$ and Si (Eqs. (4)-(7)) in anode. The charge balance needs to be considered for both $C_6$ and Si (Eqs. (11) and (12)).

### 2.1.2. Mechanical model

Li insertion and extraction are usually accompanied by volumetric changes in the active materials [49,50]. Li concentration gradient built inside active particles causes the DIS inside particles, which is the driving force for particle cracks, breakages, and isolations. From the particle level, DIS is treated analogously to thermal stress [51]. The mechanical stresses in a spherical coordinate can be written by Eqs. (25)-(27)

$$\sigma_{r,m}(r_m) = \frac{2\Omega_m E_m}{3(1-v_m)}\left[\frac{1}{R_m^3}\int_0^{R_m}\overline{c}_{1,m}r_m^2 dr_m - \frac{1}{r_m^3}\int_0^{r_m}\overline{c}_{1,m}r_m^2 dr_m\right],\qquad(25)$$

$$\sigma_{\theta,m}(r_m) = \frac{\Omega_m E_m}{3(1-v_m)}\left[\frac{2}{R_m^3}\int_0^{R_m}\overline{c}_{1,m}r_m^2 dr_m + \frac{1}{r_m^3}\int_0^{r_m}\overline{c}_{1,m}r_m^2 dr_m - \overline{c}_{1,m}\right],\qquad(26)$$
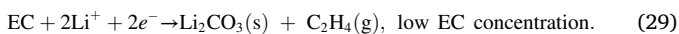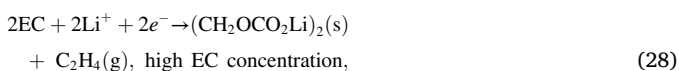
$$\sigma_{h,m}(r_m) = \frac{\sigma_{r,m}(r_m) + 2\sigma_{\theta,m}(r_m)}{3},\qquad(27)$$

where $\sigma_{r,m}$, $\sigma_{\theta,m}$ and $\sigma_{h,m}$ denote the radial, tangential, and hydrostatic stress, respectively. Note that the subscript $m$ represents C or Si. $\Omega_m$ is the partial molar volume, $E_m$ is Young's modulus, $v_m$ is the Poisson's ratio, $\overline{c}_{1,m}$ denotes the difference of Li-concentration with the reference concentration, *i.e.* $\overline{c}_{1,m} = c_{1,m} - c_{1,m}^0$. This stress model can be combined with the P2D model to predict the stress inhomogeneity in batteries [27, 39,52].

### 2.2. Aged cells

#### 2.2.1. SEI formation

SEI formation is involved in the possible reduction of ethylene carbonate (EC) based electrolyte with two-electron transferred reactions at the surface of the graphite-based anode [25,53,54], as shown in Eqs. (28) and (29)

$$2EC + 2Li^+ + 2e^- \rightarrow (CH_2OCO_2Li)_2(s)$$
$$+ \ C_2H_4(g), \ \text{high EC concentration},\qquad(28)$$

$$EC + 2Li^+ + 2e^- \rightarrow Li_2CO_3(s) + C_2H_4(g), \ \text{low EC concentration}.\qquad(29)$$

Electron tunneling is considered the rate-determining step of SEI growth. According to Ref. [26], the electron tunneling rate at the surface of $C_6$ and Si can be expressed as Eqs. (30) and (31).

$$j_{SEI,C} = j_{tl,C} = \frac{(6+y)\rho_C}{4M_C}\nu_e P_0\exp\left(-\frac{2l_{tot,C}^{in}\sqrt{2m_e\Delta E_C}}{\hbar}\right),\qquad(30)$$

$$j_{SEI,Si} = j_{tl,Si} = \frac{(4+z)\rho_{Si}}{4M_{Si}}\nu_e P_0\exp\left(-\frac{2l_{tot,Si}^{in}\sqrt{2m_e\Delta E_{Si}}}{\hbar}\right),\qquad(31)$$

where

$$l_{tot,m}^{in} = l_{0,m}^{in} + l_{inc,m}^{in}, \ m = \text{C or Si}.\qquad(32)$$

Note that $j_{SEI,m}$ ($m$ = C or Si, mol m$^{-2}$ s$^{-1}$) has a position dependency along the $x$-direction of the P2D model. The increased thickness of the inner SEI ($l_{tot,m}^{in}$) is the accumulated result of $j_{SEI,m}$. Therefore, the following equations are applied to relate $l_{tot,m}^{in}$ and $j_{SEI,m}$. Considering only part of the electron tunneling current forms the inner SEI, the percentage is defined as $\delta_m^{in}$. Therefore, the reaction rate corresponding to inner SEI growth is $\delta_m^{in}j_{SEI,m}$. The inner SEI thickness can be expressed as $\delta_m^{in}l_{SEI,m}$

$$\frac{dl_{tot,m}^{in}}{dt} = \frac{dl_{inc,m}^{in}}{dt} = \frac{\delta_m^{in}j_{SEI,m}M_{SEI}^{in}}{2\rho_{SEI}^{in}},\qquad(33)$$

where $M_{SEI}^{in}$ is the molar mass of the inner SEI and $\rho_{SEI}^{in}$ the gravimetric density of inner SEI. Note that the reaction rate of SEI growth needs to divide by 2 due to the two-electron transfer in Eqs. (28) and (29).

The loss of lithium caused by SEI formation can be derived as follows

$$\frac{dN_{SEI,C}^{Li}}{dt} = a_C j_{SEI,C},\qquad(34)$$

$$\frac{dN_{SEI,Si}^{Li}}{dt} = a_{Si} j_{SEI,Si},\qquad(35)$$

where $N_{SEI,m}^{Li}$ (mol m$^{-3}$) denotes the loss of Li due to the SEI formation at the surface of $C_6$ and Si. For convenience, here define $B_C = \frac{(6+y)\rho_C}{4M_C}\nu_e$, $B_{Si} = \frac{(4+z)\rho_{Si}}{4M_{Si}}\nu_e$, $G_m = \frac{\sqrt{2m_e\Delta E_m}}{\hbar}$, and $H_m = \frac{\delta_m^{in}M_{SEI}^{in}}{2\rho_{SEI}^{in}}$. Substitution of Eqs. (30) and (31) into Eqs. (34) and (35) yields

$$\frac{dN_{SEI,C}^{Li}}{dt} = a_C B_C P_0\exp\left(-2l_{tot,C}^{in}G_C\right),\qquad(36)$$

$$\frac{dN_{SEI,Si}^{Li}}{dt} = a_{Si} B_{Si} P_0\exp\left(-2l_{tot,Si}^{in}G_{Si}\right).\qquad(37)$$

Eq. (33) can be rewritten considered Eqs. (34) and (35)

$$\frac{dl_{tot,m}^{in}}{dt} = \frac{H_m}{a_m}\frac{dN_{SEI,m}^{Li}}{dt}.\qquad(38)$$

With the initial condition of $l_{tot,m}^{in}(t=0) = l_{0,m}^{in}$ and $N_{SEI,m}^{Li}(t=0) = 0$, the integral at both sides of Eq. (38) leads to

$$l_{tot,m}^{in} - l_{0,m}^{in} = \frac{H_m}{a_m}N_{SEI,m}^{Li}.\qquad(39)$$

Substituting Eq. (39) into Eqs. (36) and (37) gives

$$\frac{dN_{SEI,C}^{Li}}{dt} = a_C B_C P_0\exp\left[-2\left(\frac{H_C}{a_C}N_{SEI,C}^{Li} + l_{0,C}^{in}\right)G_C\right],\qquad(40)$$

$$\frac{dN_{SEI,Si}^{Li}}{dt} = a_{Si} B_{Si} P_0\exp\left[-2\left(\frac{H_{Si}}{a_{Si}}N_{SEI,Si}^{Li} + l_{0,Si}^{in}\right)G_{Si}\right].\qquad(41)$$

Solving Eqs. (40) and (41) gives

$$N_{SEI,C}^{Li} = \frac{a_C}{2H_C G_C}\ln\left[2H_C G_C B_C P_0\exp\left(-2l_{0,C}^{in}G_C\right)t + 1\right],\qquad(42)$$

$$N_{SEI,Si}^{Li} = \frac{a_{Si}}{2H_{Si}G_{Si}}\ln\left[2H_{Si}G_{Si}B_{Si}P_0\exp\left(-2l_{0,Si}^{in}G_{Si}\right)t + 1\right].\qquad(43)$$

Back substitution of $B_m$, $G_m$ and $H_m$ into Eqs. (42) and (43) gives

$$N_{\text{SEI,C}}^{\text{Li}} = \frac{a_\text{C}\rho_{\text{SEI}}^{in}\hbar}{\delta_\text{C}^{in}M_{\text{SEI}}^{in}\sqrt{2m_e\Delta E_\text{C}}}\ln\left[\frac{(6+y)\rho_\text{C}\nu_e}{4M_\text{C}}\frac{\delta_\text{C}^{in}M_{\text{SEI}}^{in}}{\rho_{\text{SEI}}^{in}}\frac{\sqrt{2m_e\Delta E_\text{C}}}{\hbar}P_0\exp\left(\frac{-2l_{0,\text{C}}^{in}\sqrt{2m_e\Delta E_\text{C}}}{\hbar}\right)t+1\right], \tag{44}$$

$$N_{\text{SEI,Si}}^{\text{Li}} = \frac{a_{\text{Si}}\rho_{\text{SEI}}^{in}\hbar}{\delta_{\text{Si}}^{in}M_{\text{SEI}}^{in}\sqrt{2m_e\Delta E_{\text{Si}}}}\ln\left[\frac{(4+z)\rho_{\text{Si}}\nu_e}{4M_{\text{Si}}}\frac{\delta_{\text{Si}}^{in}M_{\text{SEI}}^{in}}{\rho_{\text{SEI}}^{in}}\frac{\sqrt{2m_e\Delta E_{\text{Si}}}}{\hbar}P_0\exp\left(\frac{-2l_{0,\text{Si}}^{in}\sqrt{2m_e\Delta E_{\text{Si}}}}{\hbar}\right)t+1\right]. \tag{45}$$

The capacity loss caused by the SEI formation at $C_6$ and Si particle can be calculated, according to

$$Q_{\text{SEI}}^{\text{Li}} = V\left(N_{\text{SEI,C}}^{\text{Li}} + N_{\text{SEI,Si}}^{\text{Li}}\right), \tag{46}$$

where $V$ is the volume of the electrode. Another important question that needs to be stressed is the resistance of the SEI, according to

$$R_{film,m} = \frac{l_{\text{SEI},m}}{\kappa_{\text{SEI},m}}, \tag{47}$$

where $l_{\text{SEI},m}$ is the thickness of the SEI film, including the inner ($l_{tot,m}^{in}$) and outer ($l_{tot,m}^{out}$) SEI, which can be determined by Eqs. (33) and (38). $\kappa_{\text{SEI},m}$ represents the ionic conductivity of SEI.

### 2.2.2. Loss of active material (LAM)

With repeated (de)lithiation, particles endure periodical volume expansion and contraction, causing particle crack and fracture. The maximum stress and strain energy have been implemented as an indicator of LAM [27,30,39,40], and the stress and strain energy level increase as the applied C-rates increase. However, all these methods involve empirical parameters, which highly rely on parameter fitting because of the difficulties in the experimental measurements. Due to the multiple empirical parameters needed, parameter fitting is a highly time-consuming process. To simplify this process, LAM is directly related to the applied current and time [47], and only one parameter for a single active material needs to be optimized according to

$$\frac{d\varepsilon_m}{dt} = k_{\text{LAM},m}|I|, \tag{48}$$

where $\varepsilon_m$ is the volume ratio of active material $C_6$ or Si, $I$ is the applied current density, and $k_{\text{LAM},m}$ is the rate of LAM for $C_6$ or Si. The capacity loss caused by LAM is related to the state-of-charge (SoC) when the particles are subjected to losses

$$\frac{dQ_{\text{LAM},m}}{dt} = \frac{d\varepsilon_m}{dt}\cdot\text{SoC}\cdot V\cdot c_{\max,m}. \tag{49}$$

Not only the capacity loss caused by LAM, but the specific area for electrochemical reactions will also decrease according to
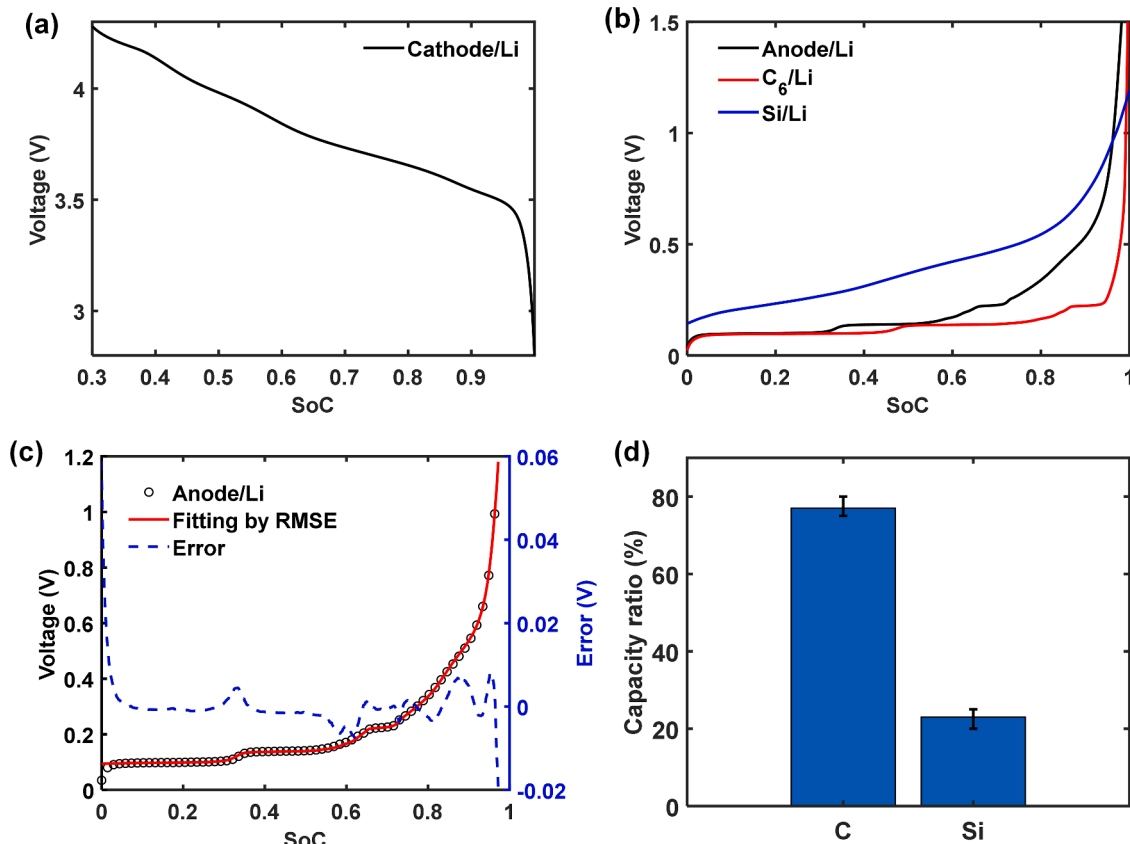


**Fig. 2.** The OCV curves of (a) cathode/Li and (b) anode/Li. The OCV curves of $C_6$/Li and Si/Li are also given to compare to that of anode/Li in (b). The OCV curve of $C_6$/Li is approximated by measuring with a 0.01C current, and the OCV curve of Si/Li is obtained from Ref. [57]. (c) Comparison between experimental (black symbols) and fitting (red line) OCV curves of anode/Li. (d) The capacity ratio of $C_6$/Si obtained from the fitting process.
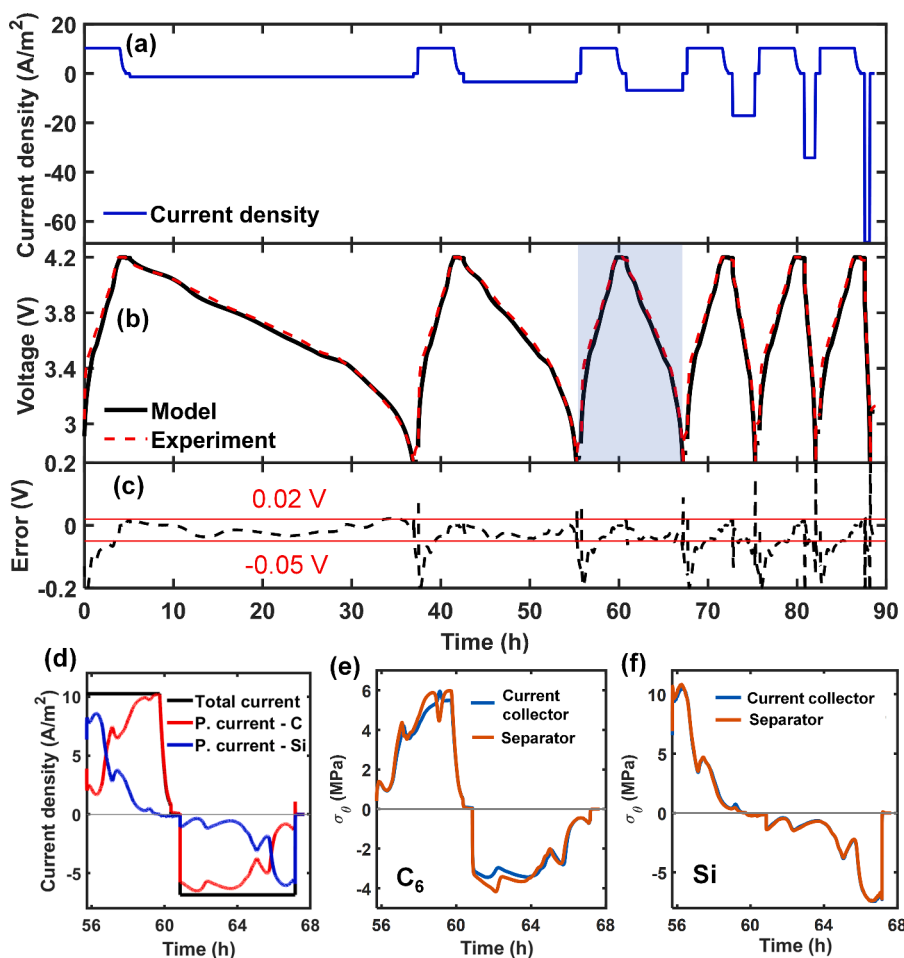
**Fig. 3.** (a) Current density used in the simulations of the characterization cycles at 25°C, which use 0.3C charge current and a set of discharge currents including 0.04, 0.1, 0.2, 0.5, 1, and 2C. Each cycle consists of a CC charge, CV charge, rest, CC discharge, and rest. (b) The simulated (black line) and experimental (red dash line) voltage curves at various C-rates. (c) The voltage error between simulation and experiment in (b). (d) The partial current densities through $C_6$ and Si in the anode at the selected cycle of 0.3C charge and 0.2C discharge, which is indicated by the blue shaded area in (b). The tangential stress at surfaces of (e) $C_6$ and (f) Si particles at the current collector and separator interfaces.

$$\frac{da_m}{dt} = \frac{3}{R_m} \cdot \frac{d\varepsilon_m}{dt}. \tag{50}$$

## 3. Experimental

### 3.1. Electrode pseudo-open-circuit voltage measurements

Pristine commercial 18650-type cylindrical batteries were dismantled in an argon-filled glove box. Pieces of the anodes and cathodes were cut out. Before measurements, one side of the double-coated anodes and cathodes were carefully removed with the help of acetone and a sharp blade. Then, the remainder was cleaned with dust-free tissues immersed in acetone. Subsequently, the electrodes were cut into discs with a diameter of 14 mm. Anode and cathode discs were assembled separately into 2032-type button cells with metallic Li as counter electrodes. A 2400-type Celgard separator (thickness 25 µm) and 1 M lithium hexa-fluorophosphate (LiPF$_6$) electrolyte in the solvent mixture of EC: dimethyl carbonate (DMC): diethyl carbonate (DEC) with a 1:1:1 volume ratio were used. For convenience, these button cells are denoted as cathode/Li and anode/Li cells.

The electrochemical properties of the button cells were measured by a Neware battery cycler in the voltage range of 0.01 – 2 V for anode/Li and 2.8 – 4.3 V for cathode/Li at 25°C. Before each test, the cells were equilibrated for 12 h and then activated for four cycles with a 0.2 C-rate current (1C = 7 mA or 45.5 A/m$^2$). Subsequently, the pseudo-open-circuit voltage (OCV) was obtained at a 0.01 C-rate current also at 25°C.

### 3.2. Cycling measurements of cylindrical batteries

Commercial 18650-type cylindrical batteries with a nominal capacity of 3.2 Ah were used in the cycling tests. Prior to these tests, all batteries were activated for 4 cycles in constant-current constant-voltage (CCCV) charging mode and constant-current (CC) discharging mode within the voltage range of 2.7 – 4.2 V. The current of 0.3C (1C = 2.5 A) was used in CC mode. The cut-off current for CV mode was 0.04C. Subsequently, the characterization cycles were performed to obtain equilibrium voltage (EMF) or OCV curves of batteries. For the characterization cycles, batteries were charged in the CC mode at 0.3C until the cut-off voltage of 4.2 V was reached, followed by CV charging mode until the current dropped below 0.04C. Then the batteries were discharged with different C-rates (0.04, 0.1, 0.2, 0.5, 1, and 2C) with the cut-off voltage of 2.7 V. The EMF curves were obtained from a set of experimentally measured discharging voltage curves by extrapolation towards zero current [55,56].

After characterization, the cycling tests were performed with the same charging current of 0.3C (or 1C) but different discharging C-rates of 0.1, 0.5, 1, and 2C. During cycling, all batteries were charged in the CCCV mode. The discharging was performed in CC mode until 2.7 V. Relaxation of 30 min was conducted between the charging and discharging steps. The characterization cycles were performed periodically every 50 or 100 cycles during cycling. The temperatures for cycling measurements were kept at 10, 25, and 45°C.

### 3.3. Storage measurements of cylindrical batteries

Calendar storage measurements were simultaneously performed

**Table 2**

P2D-based model parameters, values, and units for pristine cells.

| Symbol | Value | Unit |
|---|---|---|
| **Positive electrode** | | |
| $\delta_p$ | 69 [a] | μm |
| $\varepsilon_p$ | 0.23 [b] | - |
| $\varepsilon_{f,p}$ | 0.02 [c] | - |
| $brugg_p$ | 1.55 [c] | - |
| $\sigma_p$ | 50 [c] | S m$^{-1}$ |
| $R_p$ | 6.5 [b] | μm |
| $c_{1,p}^{max}$ | 50488 [c] | mol m$^{-3}$ |
| $c_{1,p}^{ini}$ | $0.865 c_{1,p}^{max}$ [c] | mol m$^{-3}$ |
| $D_{1,p}$ | $4 \cdot 10^{-14}$ (10°C), $5 \cdot 10^{-14}$ (25°C), $5.5 \cdot 10^{-14}$ (45°C) [c] | m$^2$ s$^{-1}$ |
| $k_p$ | $5 \cdot 10^{-11}$ (10°C), $6 \cdot 10^{-11}$ (25°C), $7 \cdot 10^{-11}$ (45°C) [c] | m$^{2.5}$ mol$^{-0.5}$ s$^{-1}$ |
| $\alpha_p$ | 0.5 [c] | - |
| $U_p^s$ | Fig. 2a | V |
| $a_p$ | $3(1 - \varepsilon_p - \varepsilon_{f,p})/R_p$ | m$^{-1}$ |
| **Negative electrode** | | |
| $\delta_n$ | 70 [a] | μm |
| $\varepsilon_n$ | 0.25 [b] | - |
| $\varepsilon_{f,n}$ | 0.02 [c] | - |
| $brugg_n$ | 1.65 [c] | - |
| $\sigma_n$ | 1000 [c] | S m$^{-1}$ |
| $R_C$ | 11 [b] | μm |
| $R_{Si}$ | 1 [a] | μm |
| $c_{1,C}^{max}$ | 30667 [c] | mol m$^{-3}$ |
| $c_{1,C}^{ini}$ | $0.078 c_{1,C}^{max}$ [c] | mol m$^{-3}$ |
| $c_{1,Si}^{max}$ | 153920 [e] | mol m$^{-3}$ |
| $c_{1,Si}^{ini}$ | $0.15 c_{1,Si}^{max}$ [c] | mol m$^{-3}$ |
| $D_{1,C}$ | $5 \cdot 10^{-14}$ (10°C), $7 \cdot 10^{-14}$ (25°C), $1.1 \cdot 10^{-13}$ (45°C) [c] | m$^2$ s$^{-1}$ |
| $D_{1,Si}$ | $2 \cdot 10^{-14}$ (10°C), $3 \cdot 10^{-14}$ (25°C), $4 \cdot 10^{-14}$ (45°C) [c] | m$^2$ s$^{-1}$ |
| $k_C$ | $6 \cdot 10^{-12}$ (10°C), $1 \cdot 10^{-11}$ (25°C), $1.34 \cdot 10^{-11}$ (45°C) [c] | m$^{2.5}$ mol$^{-0.5}$ s$^{-1}$ |
| $k_{Si}$ | $2 \cdot 10^{-13}$ (10°C), $1 \cdot 10^{-12}$ (25°C), $1.1 \cdot 10^{-12}$ (45°C), [c] | m$^{2.5}$ mol$^{-0.5}$ s$^{-1}$ |
| $\alpha_C$ | 0.5 [c] | - |
| $\alpha_{Si}$ | 0.5 [c] | - |
| $U_C^s$ | Fig. 2b | V |
| $U_{Si}^s$ | Fig. 2b | V |
| $a_C$ | $3\varepsilon_C/R_C$ | m$^{-1}$ |
| $a_{Si}$ | $3\varepsilon_{Si}/R_{Si}$ | m$^{-1}$ |
| $\Omega_C$ | $3.1 \cdot 10^{-6}$ [d] | m$^3$ mol$^{-1}$ |
| $E_C$ | 15 [d] | GPa |
| $\upsilon_C$ | 0.3 [d] | - |
| $\Omega_{Si}$ | $4.5 \cdot 10^{-6}$ [e] | m$^3$ mol$^{-1}$ |
| $E_{Si}$ | 90 [e] | GPa |
| $\upsilon_{Si}$ | 0.28 [e] | - |
| **Separator** | | |
| $\delta_{sep}$ | 20 [a] | μm |
| $\varepsilon_{sep}$ | 0.4 [c] | - |
| $brugg_{sep}$ | 1.5 [c] | - |
| **Electrolyte** | | |
| $c_2^0$ | 1300 [b] | mol m$^{-3}$ |
| $t_+$ | 0.363 [f] | - |
| $f_\pm$ | 1 [c] | - |
| $D_2$ | $10^{-4} \cdot 10^{\left(-4.43 - \frac{54}{T - 229 - 5 \cdot 10^{-3} c_2} - 0.22 * 10^{-3} c_2\right)}$. [f] | m$^2$ s$^{-1}$ |
| $\kappa$ | $10^{-4} \cdot c_2 (-10.5 + 0.668 \cdot 10^{-3} c_2 + 0.494 \cdot 10^{-6} (c_2)^2 + 0.074T - 1.78 \cdot 10^{-5} c_2 T - 8.86 \cdot 10^{-10} (c_2)^2 T - 6.96 * 10^{-5} T^2 + 2.8 \cdot 10^{-8} c_2 T^2)^2$. [f] | S m$^{-1}$ |

[a] Measured values.
[b] Provided by the manufacturer.
[c] Estimated and optimized values from the model.
[d] Taken from Ref. [52].
[e] Taken from Ref. [57]
[f] Taken from Ref. [61].

with the cylindrical batteries. Before storage, all batteries were cycled with a 0.3C current for 50 cycles to form a stable SEI, followed by a set of characterization cycles. Subsequently, batteries were stored at 20%, 50%, and 100% of SoC at 25°C. During storage, batteries were re-characterized every 30 days. After re-characterizations, batteries were recharged to the corresponding SoC to continue the storage tests. At 10 and 45°C, batteries were stored at 50% SoC.

## 4. Results and discussion

### 4.1. Modeling pristine cell

Fig. 2a-b shows the OCV curves of cathode and anode *vs.* metallic Li measured in button cells. The active cathode material is NCA. The active materials in the anode are $C_6$ and Si. Fig. S1 shows the morphologies of the cathode and anode by Scanning Electron Microscope (SEM)
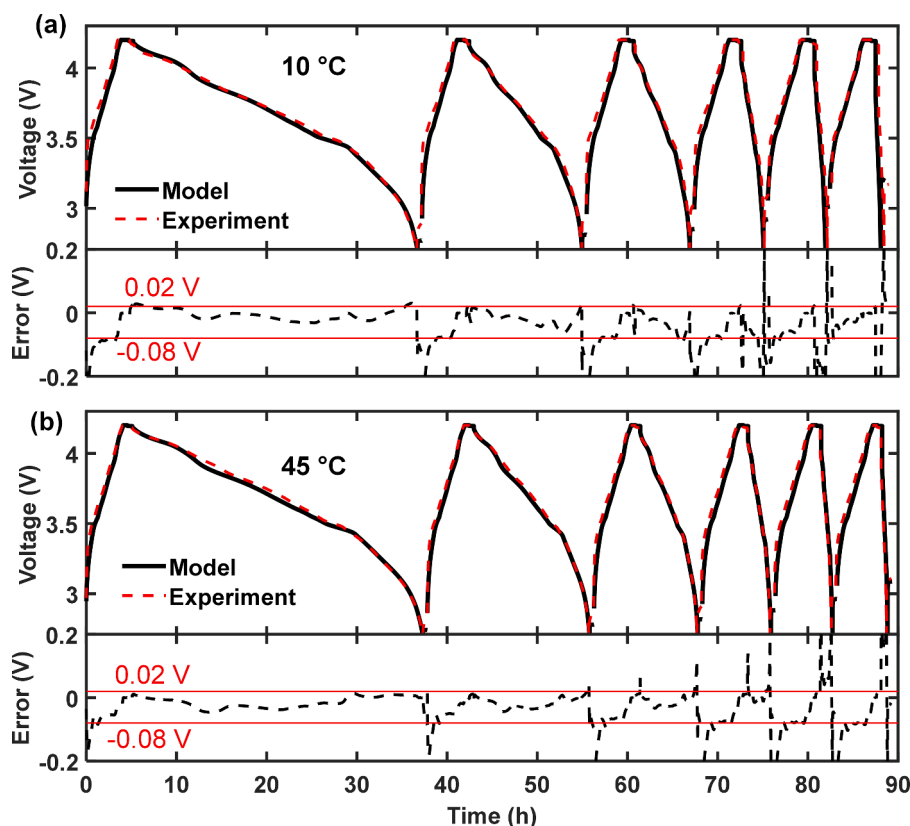
**Fig. 4.** Simulated (black line) and experimental (red dash line) voltage curves and error at various C-rates at (a) 10 and (b) 45°C.

equipped with Energy-dispersive X-ray Spectroscopy (EDX). It has been proven that both $C_6$ and Si exist inside the anode. The atomic ratio of Si/C ranges from 1.41 to 2.35% based on the EDX test. A fitting process is performed to reveal the exact mass and capacity ratios between $C_6$ and Si. The method of minimizing the root-mean-square error (RMSE) is applied. In this method, the OCV curve of anode/Li works as the fitting objective. The OCV curve of $C_6$/Li and Si/Li (shown in Fig. 2b) are combined (non)linearly to satisfy the fitting objective. The cost function of this fitting process is shown in Eq. (51)

$$\min(RMSE) = \min\left\{ \sqrt{\frac{\sum_{i=1}^n \left( \widehat{SoC_C^i}(V^i) + \widehat{SoC_{Si}^i}(V^i) - SoC_{Anode}^i(V^i) \right)}{n}} \right\},$$

(51)

where $\widehat{SoC_C^i}(V^i)$ and $\widehat{SoC_{Si}^i}(V^i)$ are the estimated SoC of $C_6$ and Si under a specific voltage $V^i$. $SoC_{Anode}^i(V^i)$ is the experimental SoC of anode/Li at $V^i$. The fitting results are shown in Fig. 2c, where symbols denote the experimental OCV of the anode, and the red line stands for the combination of the OCV of $C_6$ and Si electrodes. Good agreement can be found between the fitting result and the experiment. The fitted capacity ratio between $C_6$ and Si is shown in Fig. 2d. This ratio is used to simulate the electrochemical behavior and degradation of NCA/$C_6$-Si cells.

Fig. 3a shows the simulated current densities for the first characterization cycle set at 25°C. Each cycle includes a CC charge, CV charge, rest, CC discharge, and another rest period. The CC charge current is kept at 0.3C, followed by the CV charge and rest. The discharge current includes 0.04, 0.1, 0.2, 0.5, 1.0 and 2.0C. The parameter values used are shown in Table 2. The simulated (black solid lines) and experimental (red dash lines) voltage curves are shown in Fig. 3b. The voltage error between simulation and experiment is shown in Fig. 3c. Good agreement can be found between the simulation and experiment at all C-rates.

Since the anode consists of $C_6$ and Si, Fig. 3d shows the total current

and partial currents passing through $C_6$ and Si separately during 0.3C charge and 0.2C discharge, which is indicated by the light blue shaded area in Fig. 3b. At the beginning of charging, the partial current through Si is higher than that passing $C_6$. After that, the partial current passing through $C_6$ dominates until the end of the CC charge. This behavior indicates that Si dominates in the competing lithiation reaction at the beginning of the CC charge, while $C_6$ takes over later on. Graphite dominates the competing lithiation reaction during CV charge while nearly no current passes through Si. This observation suggests that the lithiation among Si is relatively uniform at the end of the CC charge. However, it is nonuniform at $C_6$, so the CV charge offsets the nonuniform lithiation of $C_6$. This behavior can be explained by the fact that the Si already experienced a long period with a low current from the middle to the end of charging. This period has already compensated for the nonuniform charging among Si particles. During discharging, the partial current dominates at $C_6$ from the beginning to the late stage. The partial current at Si increases from the middle to the end of discharge. This behavior suggests that $C_6$ dominates the competing delithiation reaction first during discharging, followed by the Si. Similar competing partial currents between $C_6$ and Si have previously been reported in a composite anode [58].

The OCV curves of Si (blue curve in Fig. 2b) and $C_6$ (red curve) can be used to understand this observation. The (de)lithiation plateaus of $C_6$ are below 0.23 V (vs. Li$^+$/Li), accounting for 94% of the total capacity of $C_6$. The (de)lithiation voltage interval of Si over 0.23 V takes up 81% of the total capacity of Si. It can therefore be concluded that the majority of the (de)lithiation reaction of Si occurs above 0.23 V. In contrast, the main (de)lithiation reaction of $C_6$ occurs below 0.23 V. For lithiation from a fully delithiated state, the anode voltage goes down from around 3.0 V (vs. Li$^+$/Li). The lithiation reaction will be dominant on Si until the voltage drops down to 0.23 V. Then, the lithiation reaction on $C_6$ takes over the major role until the voltage reaches the lower cutting-off voltage. The reverse sequence occurs during delithiation. This fact has
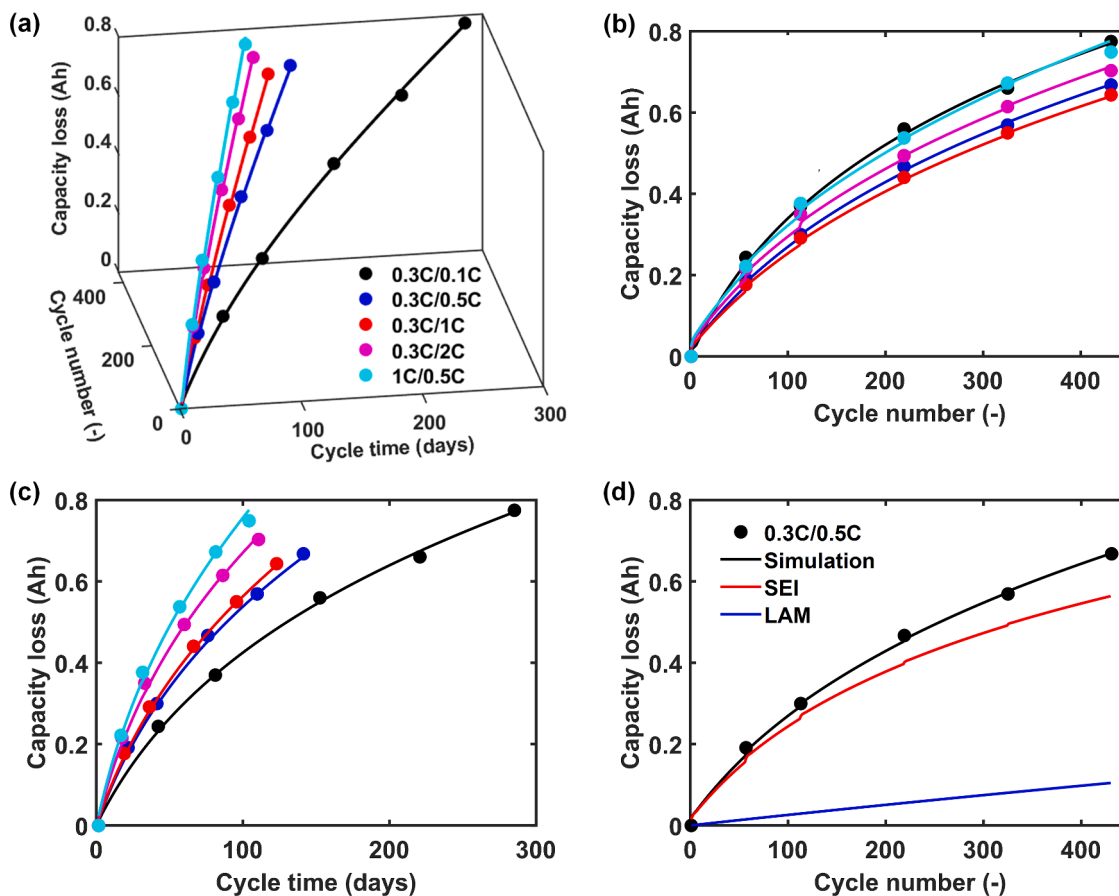
**Fig. 5.** (a) Three-dimensional (3D) representation of capacity loss at various currents as a function of cycle time and cycle number at 25°C. Two-dimensional (2D) capacity loss as a function of (b) cycle number and (c) cycle time. Symbols represent the experiment, and lines the simulated results. (d) The decomposition of total capacity loss into SEI-induced and LAM-induced capacity loss in the case of 0.3C charge and 0.5C discharge current.

**Table 3**
Values and units of constant parameters of the aging model.

| Symbol | Value | Unit |
|---|---|---|
| $\rho_C$ | $2.1 \cdot 10^6$ [a] | g m$^{-2}$ |
| $M_C$ | 72 (C$_6$) [a] | g mol$^{-1}$ |
| $\rho_{Si}$ | $2.33 \cdot 10^6$ [b] | g m$^{-2}$ |
| $M_{Si}$ | 112.4 (Si$_4$) [b] | g mol$^{-1}$ |
| $\rho_{SEI}^{in}$ | 74 [a] | g m$^{-2}$ |
| $M_{SEI}^{in}$ | $2.1 \cdot 10^7$ [b] | g mol$^{-1}$ |
| $\kappa_{SEI,C}\ \kappa_{SEI,Si}$ | $(4 \sim 7.5) \cdot 10^{-7}$ [b] | S m$^{-1}$ |
| $\delta_m^{in}$ | $4.6 \cdot 10^{-3}$ [a] | - |
| $m_e$ | $9.1 \cdot 10^{-31}$ [a] | kg |
| $\hbar$ | $1.055 \cdot 10^{-34}$ [a] | J s |

[a] Taken from Ref. [26].
[b] Estimated and optimized values from the model.

**Table 4**
Optimized parameters in the aging model.

| | $\Delta E_C$ ($\Delta E_{Si}$) (eV) | $l_{0,C}^{in}$ (nm) | $l_{0,Si}^{in}$ (nm) | $k_{LAM,C}$ (A$^{-1}$ s$^{-1}$) | $k_{LAM,Si}$ (A$^{-1}$ s$^{-1}$) |
|---|---|---|---|---|---|
| **Cycle** | | | | | |
| 0.3C/0.1C | 2.19 | 2.688 | 2.718 | $1.095 \cdot 10^{-10}$ | $4.689 \cdot 10^{-10}$ |
| 0.3C/0.5C | 2.158 | 2.688 | 2.717 | $1.211 \cdot 10^{-10}$ | $5.317 \cdot 10^{-10}$ |
| 0.3C/1C | 2.153 | 2.688 | 2.718 | $1.593 \cdot 10^{-10}$ | $5.687 \cdot 10^{-10}$ |
| 0.3C/2C | 2.124 | 2.668 | 2.717 | $2.103 \cdot 10^{-10}$ | $6.973 \cdot 10^{-10}$ |
| 1C/0.5C | 2.095 | 2.688 | 2.717 | $2.65 \cdot 10^{-10}$ | $8.004 \cdot 10^{-10}$ |
| 0.3C/0.5C @10°C | 2.252 | 2.688 | 2.717 | $4.21 \cdot 10^{-10}$ | $9.517 \cdot 10^{-10}$ |
| 0.3C/0.5C @45°C | 2.112 | 2.688 | 2.717 | $6.211 \cdot 10^{-10}$ | $1.418 \cdot 10^{-9}$ |
| **Storage** | | | | | |
| 20% | 2.35 | 2.803 | 2.832 | - | - |
| 50% | 2.2 | 2.803 | 2.83 | - | - |
| 100% | 2.142 | 2.809 | 2.846 | - | - |
| 50% @10°C | 2.26 | 2.803 | 2.823 | - | - |
| 50% @45°C | 2.093 | 2.831 | 2.851 | - | - |

Estimated and optimized values from the model.

been experimentally validated at low C-rates [59]. At intermediate and large C-rates, overpotentials start to play a significant role. The reaction will dominate at Si or C$_6$ at different voltages than at low C-rates. However, the general (de)lithiation sequence between Si and C$_6$ should be the same as the low C-rates. For example, the lithiation starts on Si from a fully delithiated state, and the delithiation starts on C$_6$ from a fully lithiated state.

The competing partial currents between Si and C$_6$ in the anode also induce a different mechanical behavior during (dis)charge. Fig. 3e and f show the tangential stress ($\sigma_\theta$) at the surface of particles for C$_6$ and Si. Two typical particles at the current collector and separator interfaces are compared. One can see that the $\sigma_\theta$ shows similar trends as the partial currents of C$_6$ and Si. During charge, $\sigma_\theta$ at C$_6$ particle surface shows

increasing trends and reaches a maximum at the end of CC charging. Si shows the maximum stress at the beginning of charging and decreases until the end of charging. During discharging, the stress behavior also shows a resemblance to partial currents. These stress behaviors are related to the Li$^+$ concentration inside particles [51,60]. When more reactions occur at Si, the stress will be larger due to diffusion, *i.e.* at the
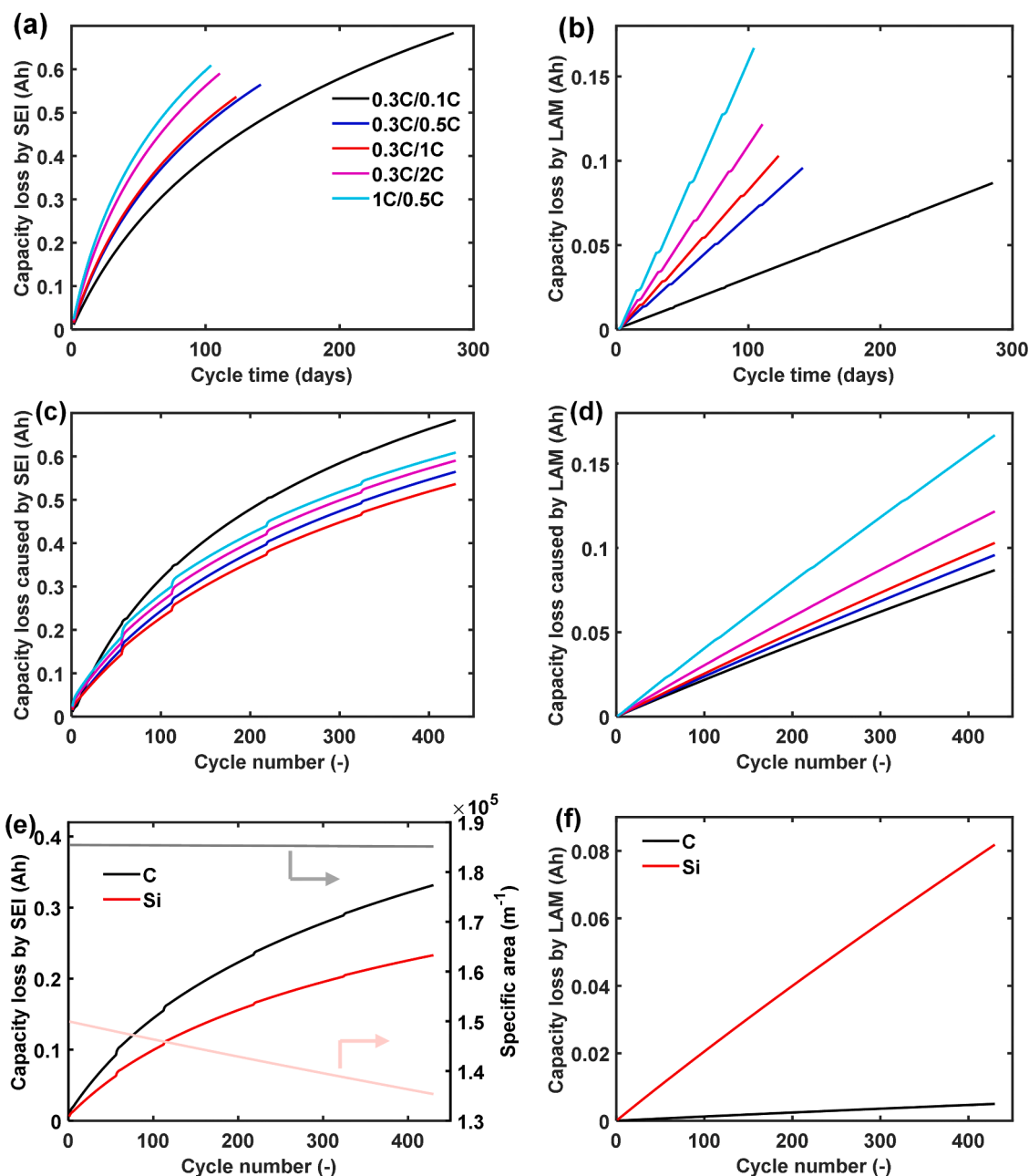
**Fig. 6.** Comparison of SEI-induced and LAM-induced capacity loss at various cycle currents as a function of (a, b) cycle time and (c, d) cycle number. The separation of (e) SEI-induced and (f) LAM-induced capacity loss for $C_6$ and Si in the case of 0.3C charge and 0.5C discharge current.

beginning of charging and the end of discharging. In addition, the stress behavior shows differences among $C_6$ particles. Particles near the separator interface show larger stress during (dis)charge. However, the stress behavior of Si particles shows fewer differences across the thickness, indicating the reaction among Si particles is relatively uniform. Fig. S2 shows the tangential stress at the particle surface for $C_6$ and Si at various C-rates. Large C-rates cause elevated stress levels at both $C_6$ and Si particles.

Fig. 4 shows the simulated (black line) and experimental (red dash line) voltage curves and the corresponding voltage error at various C-rates at 10 (a) and 45°C (b). It can be seen that simulations fit very well with the experiments at the reduced and elevated temperatures. At elevated temperatures, the discharge voltage curves are higher than those at low temperatures due to a reduced overpotential (Fig. S3). Additionally, the accelerated diffusion at the high temperatures makes the Li$^+$ concentration gradient lower than that at a lower temperature,

resulting in a depressed stress (Fig. S4). The parameters achieving good voltage fit in Figs. 3 and 4 will be used to model aging behavior in the next sections.

### 4.2. Modeling cycle-induced degradation at different currents

Fig. 5a gives a three-dimensional (3D) view of battery capacity loss at various cycling currents as a function of cycle time and cycle number. The parameter values used are presented in Tables 2,3,4. The cycling conditions include 0.3C charge current followed by 0.1, 0.5, 1 and 2C discharge currents, and 1C charge current followed by 0.5C discharge current. The symbols show the experimental discharge capacity loss, which is extracted through a combination of interpolation and extrapolation on a set of discharge voltage curves [43,44,62,63]. Figs. S5 and S6 show an example of this method, where the interpolation and extrapolation are applied to each characterization cycle set. The
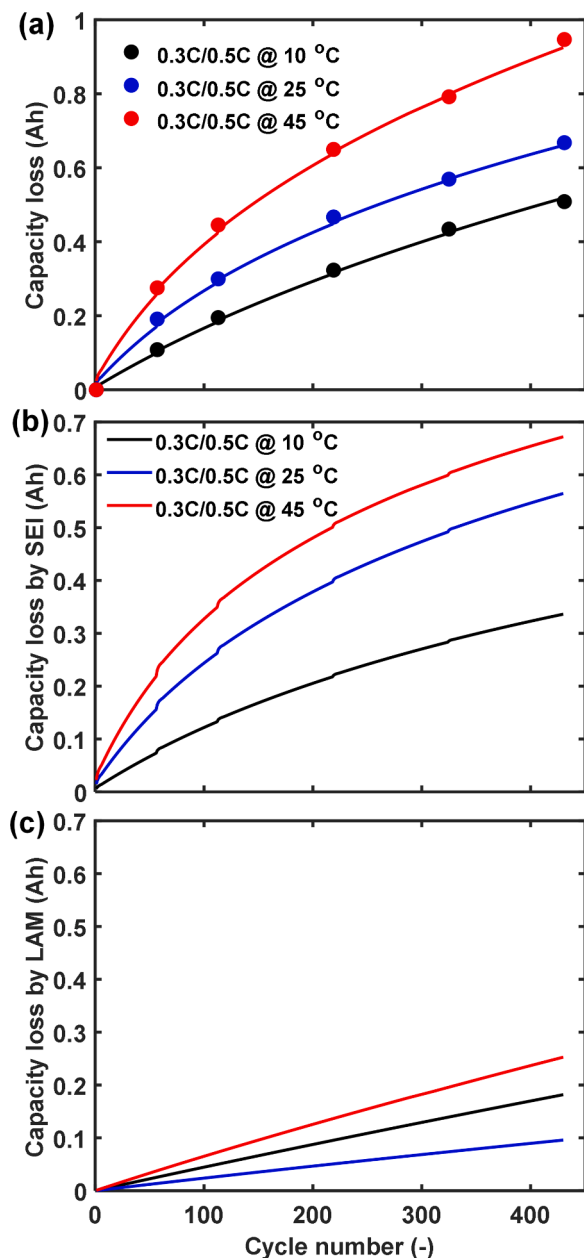
**Fig. 7.** (a) Total capacity losses during cycling at 10, 25, and 45°C. Separation of (b) SEI-induced and (c) LAM-induced capacity losses. The symbols represent the experimental results, and the lines represent the simulations.

capacity loss is extracted subsequently. The lines in Fig. 5a are the simulated results with the SEI growth model and LAM model implemented. The capacity loss and discharge voltage curves up to the first 5 characterization cycle sets are used to minimize the fit error using the RMSE method. The applied cost function is shown in Eq. (52)

$$
f = \min \left\{ \beta \cdot \sum \left( Q_{loss}^{exp} - Q_{loss}^{sim} \right)^2 + (1-\beta) \cdot \sum_{Crate} \sum_{i=1}^{n} \frac{\left( V_{Crate}^{i,sim} - V_{Crate}^{i,exp} \right)^2}{n} \right\},
$$

(52)

where $Q_{loss}^{exp}$ and $Q_{loss}^{sim}$ are the experimental and simulated capacity loss, $V_{Crate}^{i,exp}$ and $V_{Crate}^{i,sim}$ are the experimental and simulated voltage at the voltage vector $i$, and $\beta$ is a weight factor regulating the fit results favorable for the capacity loss or voltage curves. The capacity loss fit is presented in Fig. 5a. Fig. S7 shows the experimental and simulated voltage curves of the case of 0.3C charge and 0.5C discharge as an example, where a reasonably good fit can be found for the selected cycles in each characterization cycle set. In Fig. 5a, the capacity loss obtained from the 6th characterization set is also plotted to examine the fitted processes, revealing a great alignment.

Fig. 5b and c give two-dimensional (2D) views of the capacity loss as a function of cycle number and cycle time, as the projections of 3D curves in Fig. 5a. Obviously, the capacity loss increases with both the cycle number and time at all currents. The capacity loss behaves irregularly with currents at the same cycle number (Fig. 5b). The case of low C-rate discharge (0.3C/0.1C) shows the largest capacity loss. In contrast, the case of mediate C-rate discharge (0.3C/1C) shows the lowest capacity loss. The largest discharge current (0.3C/2C) shows the intermediate capacity loss, and the case of 0.3C/0.5C shows the second lowest capacity loss. In particular, the large charge current (1C/0.5C) shows almost the same capacity loss as the case of low C-rate discharge (0.3C/0.1C).

At the same cycling time (Fig. 5c), the capacity loss shows a dependence on the cycling current. A large discharge current incurs a large capacity loss. On the contrary, low discharge current results in less capacity loss. Also, the large charge current causes even more capacity losses. These are because batteries with large cycling currents undergo more equivalent full cycles than those with small cycling currents when keeping the cycling time the same. Even though the capacity loss at the same equivalent cycles shows irregularities with cycle currents in Fig. 5b, more cycles generally cause more capacity losses. Such behavior can always be observed with the large cycling currents when setting the cycle time the same. From Fig. 5a-c, it can be inferred that under a constant environmental temperature, battery capacity losses are the result of multifactorial effects, including cycle number, cycling time, and cycle current. In other words, the various degradation phenomena inside the battery should be influenced by the cycle number, cycling time, cycle current, and temperatures.

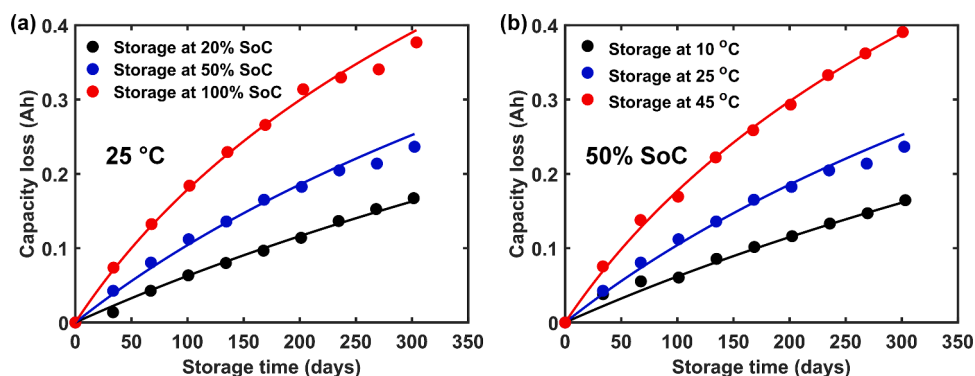Degradation in LIB originates from many physical and (electro)



**Fig. 8.** Total capacity losses during storage at various (a) SoC and (b) temperatures.

chemical mechanisms. These mechanisms cause a loss of lithium inventory (LLI) and LAM [18,20,64-70]. In the presented model, the SEI formation is considered the main reason for LLI. Loss of $C_6$ and Si active materials is the reason for LAM. SEI formation and LAM models are integrated into the P2D model as described in Section 2.2. With the fitting process, the capacity loss induced by SEI and LAM can be extracted separately. Fig. 5d shows an example of the capacity loss caused by SEI and LAM in the case of 0.3C/0.5C. The extractions at other cycling currents are shown in Fig. S8. In all these cases, the SEI-induced capacity loss takes the major role.

In contrast, LAM takes only a small portion of the total capacity loss. Previously, it has been demonstrated that Li loss plays a primary role in the deterioration of cell performance rather than the LAM [22,71,72]. Some publications considered capacity loss solely caused by SEI growth [26,73-75] or the combination of SEI growth and Li plating [21,76]. They also successfully explained the battery capacity loss for long-time cycling. These again demonstrate the dominant effect of SEI on the total capacity loss. LAM happens during cycling, but it does not cause significant capacity losses.

Fig. 6a-d show the decoupled capacity loss caused by SEI and LAM as a function of cycle time and cycle number. It can be seen that SEI growth correlates positively with the cycling current under a specific cycling time but does not show a dependence on cycling current at a given cycle number. LAM reveals a positive relationship with cycling at a given cycle time or cycle number. These observations suggest that SEI is influenced by the cycle time, cycle number, and cycle current. LAM is influenced mainly by the cycling current.

As reported in literature, SEI growth depends on time, currents, and SoC [77–79] at a constant temperature. A high current causes a short cycling time. A low cycling current obviously has a longer cycling time and causes a more extensive SEI-induced capacity loss [77].

In addition, the SEI formed at low currents is monolithic and amorphous. In contrast, a high current leads to a thick mosaic-structured SEI [78]. Therefore, both the long cycle times and large cycle currents accelerate the SEI growth. However, when a specific cycling condition is considered, these two factors generally oppose each other with respect to SEI growth. That is why SEI growth shows positive dependency on cycling current under a certain cycle time but does not show obvious dependence on cycling current under a certain cycle number in Fig. 6a and c. Also, SEI grows faster during charge than discharge, even at the same current [77]. This phenomenon causes a large battery capacity loss with a high charging C-rate. The stress generated by diffusion is an essential source of LAM. The low stress levels at low currents cause low LAM. The high current generates high stress, causing large LAM. The cycling time does not have a critical effect on LAM.

Fig. S9 shows the percentages of SEI and LAM in the total capacity loss as a function of cycle numbers at various cycling currents. Table S1 shows the percentage of SEI-induced and LAM-induced capacity losses at the selected cycles. Even though the capacity loss in Fig. 5b does not show regularities with cycle currents, the percentages of SEI and LAM in Fig. S9 show a proportional relationship with cycle currents. With the lowest discharge currents, the percentage of SEI takes the largest part of total capacity loss, and LAM accounts for the lowest portion. For example, SEI-induced capacity losses take up 89, 86, 84, and 83% for 0.1, 0.5, 1, and 2C discharging currents at the end of the 400th cycle, and LAM-induced capacity losses account for 11, 14, 16, and 17% of the total capacity losses. With higher discharge currents, SEI takes a lower part, and LAM accounts for a higher portion of the total capacity loss. Large charge currents, on the contrary, cause a large LAM percentage and a small SEI portion.

The anode used in batteries is composed of $C_6$ and Si. SEI can grow both on the surface of $C_6$ and Si. Fig. 6e shows the separate SEI-induced capacity loss from $C_6$ and Si for the cycling current of 0.3C charge and 0.5C discharge. Due to the lack of details on electron tunneling on $C_6$ and Si, it is thought that the electron tunneling barriers for $C_6$ and Si are the same, *i.e.* $\Delta E_{Si} = \Delta E_C$. Therefore, only the surface area and the Li

content inside the material influence the SEI formation rate, as suggested by Eqs. (44)-(45). Due to the larger surface areas of $C_6$, the capacity loss caused by SEI growth on $C_6$ is higher than that on Si at the beginning, as shown in Fig. 6e. In addition, the fast degradation of Si makes the active surface area decrease faster than $C_6$, implying a higher SEI growth rate on $C_6$ during cycling in Fig. 6e. Fig. 6f shows the capacity loss caused by LAM from $C_6$ and Si separately. It can be seen that capacity loss caused by Si active material degradation is much larger than that of $C_6$.

### 4.3. Modeling cycle-induced degradation at different temperatures

Fig. 7a shows the cycle-induced total capacity loss at 10, 25, and 45°C, in which 0.3C charge and 0.5C discharge currents are applied. It can be seen that the total capacity loss increases positively with temperatures. At 10°C, the battery shows less capacity loss compared to that at 25°C, while the battery shows an enlarged capacity loss at 45°C. Fig. 7b and c give the individual capacity loss caused by SEI growth and LAM under three different temperatures. Table S2 shows the percentage of SEI-induced and LAM-induced capacity losses at selected cycles. Clearly, capacity loss caused by SEI is the dominant factor at all temperatures. With the temperature increase, SEI-induced capacity loss also increases due to a high electron tunneling rate at high temperatures [45]. At low temperatures, the depressed diffusion coefficient leads to a higher DIS since a larger Li concentration gradient inside particles. On the contrary, high temperatures will cause a lower level of DIS. In Fig. 7c, LAM at 10°C shows a higher degradation, as expected from a higher stress level. However, at high temperatures, LAM shows an even higher degradation, which seems to violate from the DIS level. Many reasons could be responsible for this observation. The literature shows that side reactions at the anode side are accelerated at high temperatures [80]. The generated thicker SEI film has a higher possibility of isolating active particles. The deposition of transition metal, dissolved from the cathode and transported to the anode side, could also block the active site for (de)lithiation [44,45,63]. This dissolution and deposition are accelerated at high temperatures. All these reasons can cause a higher degradation of LAM at elevated temperatures.

### 4.4. Modeling storage-induced degradation

Fig. 8 gives the capacity loss during calendar storage at various SoC (a) and temperatures (b). The capacity loss caused by LAM during cycling remains minor. During storage, active materials in batteries do not experience repeated (de)lithiation except for the characterization cycles, which remain a small portion of the total storage period. Therefore, it is believed that the capacity loss is mainly caused by SEI formation to simplify the calculation. The aging model in this part only considers the SEI growth. In the literature, SEI growth is also considered the main reason for battery capacity loss during storage [81,82].

The capacity loss of batteries stored at various SoC at 25°C is plotted in Fig. 8a. Table S3 shows the percentage of capacity losses with respect to the total capacity on selected days. The symbols in Fig. 8a represent the capacity loss extracted from experiments, and the lines are the simulation results. Good agreement can be found between experiment and simulation at all storage SoC. It also can be seen that storage-induced capacity loss is sensitive to SoC. After 300 days of storage, the batteries lose 5, 8, and 13% of the total capacity at 20, 50, and 100% SoC storage (Table S3). Storage with high SoC shows a large capacity loss. Contrarily, storage with low SoC shows a lower capacity loss. At high SoC, the lithiation states of the $C_6$ and Si are high, and the electron tunneling barrier energy is relatively low. Together, these two factors cause a higher electron tunneling rate at high SoC, eventually resulting in a high battery capacity loss.

Fig. 8b shows battery capacity loss during storage at different temperatures, and the SoC is kept at 50%. Likewise, high temperature induces a high capacity loss, and low temperature brings a low capacity

loss. After 300 days of storage, the batteries show 5, 8, and 13% of the total capacity losses at 10, 25, and 45°C storage temperatures (Table S3). Due to SEI growth is (electro)chemical reactions, which show positive temperature dependency. In the present paper, the electron tunneling process is considered the rate-determining step of SEI formation. The energy barrier is depressed at high temperatures, resulting in a higher electron tunneling rate and SEI-induced capacity loss [45]. In addition, SEI can grow on the surface of both $C_6$ and Si. The larger initial surface area of $C_6$ also introduces more storage-induced capacity loss than Si.

In this manuscript, a full order P2D porous electrode model is combined with aging models to simulate the pristine and aged NCA/$C_6$-Si cells. First, the electrochemical behavior of pristine cells has been studied. Then the factors causing capacity losses have been identified in storage and cycling experiments. This model can also be applied in control-related studies, such as SoC and state-of-health (SoH) estimation and real-time temperature indication with the help of state observers [83]. In addition, the reduced-order electrochemical model is also extensively used for battery status indication and cycle-life assessment [84]. One of the most popular reduced-order models is the single particle model (SPM), in which a single particle is used to represent a porous electrode in terms of electrochemical modeling [84]. Compared to the full order P2D model, SPM can significantly reduce computation complexity and increase calculation efficiency. Aging models can also be coupled to the SPM model to simulate degradation. SPM-model-equipped aging models are less complex and faster than the full order P2D model.

Moreover, the P2D model coupled with aging models can also be used to provide a strategy for optimal aging-aware charging, a similar approach as applied in ECM-based models [85]. Some publications have already implemented P2D and aging models for optimal charging with the reduction of aging as target [86,87]. As proposed, the P2D model is built together with the aging models, *i.e.* SEI growth and Li plating, to present a model-based design method for multi-stage charging protocols. This model-based method makes a trade-off between charging time and battery aging to achieve an extended battery lifetime. It is expected that such an approach will help to improve the accuracy and predictive power. However, it is computationally demanding because many parameters must be estimated in the full-order P2D and electron-tunneling-based SEI growth models. Proper model reduction would be beneficial, for example, adopting suitable simplification of equations and optimized calculations [88].

## 5. Conclusion

In the present paper, a P2D-based model has been developed for cylindrical Li-ion batteries with NCA cathodes and $C_6$/Si blended anodes, in which Si contributes to around 20% of the total capacity. Integrated with SEI growth and LAM models, the P2D-based model can be applied to simulate cycle-induced and storage-induced capacity losses. Within the framework of the P2D-based model, the electrochemical properties of the pristine NCA/$C_6$-Si are investigated. During charging from a fully delithiated state, the lithiation reaction starts from Si, followed by $C_6$. In contrast, delithiation commences at $C_6$, followed by Si during discharging from a fully lithiated state. According to this behavior, different partial currents pass Si and $C_6$, eventually affecting the stress in both materials. SEI growth causes a dominant capacity loss for aged cells at various cycling currents and temperatures. LAM also induces capacity loss but does not play a critical role. At the end of the 400th cycle, SEI-induced capacity losses take up 89, 86, 84, and 83% of the total capacity losses for 0.1, 0.5, 1, and 2C discharging currents, respectively. SEI growth depends on the cycle time, cycle current, cycle number, and temperature. LAM is most influenced by the cycle current and temperatures. SEI growth is considered the main reason for battery capacity loss during calendar aging. It is influenced by the storage time, storage SoC and temperatures. After 300 days of storage, the batteries show 5, 8, and 13% of the total capacity loss at 20, 50, and 100% SoC

storage, respectively, at 25°C. At 50% storage SoC, the batteries show 5, 8, and 13% of the total capacity loss at 10, 25, and 45°C storage temperature, respectively.

## Declaration of Competing Interest

The authors declare that they have no known competing financial interests or personal relationships that could have appeared to influence the work reported in this paper.

## Data availability

Data will be made available on request.

## Supplementary materials

Supplementary material associated with this article can be found, in the online version, at doi:10.1016/j.electacta.2022.141077.

## References

[1] X. Zhang, Z. Ju, Y. Zhu, K.J. Takeuchi, E.S. Takeuchi, A.C. Marschilok, G. Yu, Adv. Energy Mater. (2020), 2000808.
[2] D. Andre, S.-J. Kim, P. Lamp, S.F. Lux, F. Maglia, O. Paschos, B. Stiaszny, J. Mater. Chem. A 3 (2015) 6709–6732.
[3] S.-T. Myung, F. Maglia, K.-J. Park, C.S. Yoon, P. Lamp, S.-J. Kim, Y.-K. Sun, ACS Energy Lett. 2 (2016) 196–223.
[4] H. Wang, S. Frisco, E. Gottlieb, R. Yuan, J.F. Whitacre, J. Power Sources 426 (2019) 67–73.
[5] Y. Preger, H.M. Barkholtz, A. Fresquez, D.L. Campbell, B.W. Juba, J. Romàn-Kustas, S.R. Ferreira, B. Chalamala, J. Electrochem. Soc. 167 (2020) 120532.
[6] M. Endo, C. Kim, K. Nishimura, T. Fujino, K. Miyashita, Carbon 38 (2000) 183–197.
[7] S. Flandrois, B. Simon, Carbon 37 (1999) 165–180.
[8] M.N. Obrovac, L.J. Krause, J. Electrochem. Soc. 154 (2007) A103.
[9] U. Kasavajjula, C. Wang, A.J. Appleby, J. Power Sources 163 (2007) 1003–1039.
[10] J. Tang, A.D. Dysart, D.H. Kim, R. Saraswat, G.M. Shaver, V.G. Pol, Electrochim. Acta 247 (2017) 626–633.
[11] Z. Wen, J. Yang, B. Wang, K. Wang, Y. Liu, Electrochem. Commun. 5 (2003) 165–168.
[12] Z. Luo, D. Fan, X. Liu, H. Mao, C. Yao, Z. Deng, J. Power Sources 189 (2009) 16–21.
[13] Y. Xu, Y. Zhu, C. Wang, J. Mater. Chem. A 2 (2014) 9751–9757.
[14] I. Sturm, A. Rheinfeld, I. Zilberman, F.B. Spingler, S. Kosch, F. Frie, A. Jossen, J. Power Sources 412 (2019) 204–223.
[15] I. Zilberman, J. Sturm, A. Jossen, J. Power Sources 425 (2019) 217–226.
[16] H. Li, C. Liu, X. Kong, J. Cheng, J. Zhao, J. Power Sources 438 (2019), 226971.
[17] X. Li, A.M. Colclasure, D.P. Finegan, D. Ren, Y. Shi, X. Feng, L. Cao, Y. Yang, K. Smith, Electrochim. Acta 297 (2019) 1109–1120.
[18] D. Anseán, G. Baure, M. González, I. Cameán, A.B. García, M. Dubarry, J. Power Sources 459 (2020), 227882.
[19] M.R. Palacin, Chem. Soc. Rev. 47 (2018) 4924–4933.
[20] C.R. Birkl, M.R. Roberts, E. McTurk, P.G. Bruce, D.A. Howey, J. Power Sources 341 (2017) 373–386.
[21] X.-G. Yang, Y. Leng, G. Zhang, S. Ge, C.-Y. Wang, J. Power Sources 360 (2017) 28–40.
[22] J. Wang, J. Purewal, P. Liu, J. Hicks-Garner, S. Soukazian, E. Sherman, A. Sorenson, L. Vu, H. Tataria, M.W. Verbrugge, J. Power Sources 269 (2014) 937–948.
[23] A. Barré, B. Deguilhem, S. Grolleau, M. Gérard, F. Suard, D. Riu, J. Power Sources 241 (2013) 680–689.
[24] E. Peled, S. Menkin, J. Electrochem. Soc. 164 (2017) A1703–A1719.
[25] A. Wang, S. Kadam, H. Li, S. Shi, Y. Qi, Npj Comput. Mater. 4 (2018) 15.
[26] D. Li, D. Danilov, Z. Zhang, H. Chen, Y. Yang, P.H.L. Notten, J. Electrochem. Soc. 162 (2015) A858–A869.
[27] J.M. Reniers, G. Mulder, D.A. Howey, J. Electrochem. Soc. 166 (2019) A3189–A3200.
[28] Y. Zhao, P. Stein, Y. Bai, M. Al-Siraj, Y. Yang, B.-X. Xu, J. Power Sources 413 (2019) 259–283.
[29] A.A. Tahmasbi, M.H. Eikerling, Electrochim. Acta 283 (2018) 75–87.
[30] A.J. Crawford, D. Choi, P.J. Balducci, V.R. Subramanian, V.V. Viswanathan, J. Power Sources 501 (2021), 230032.

[31] X. Zhang, Y. Gao, B. Guo, C. Zhu, X. Zhou, L. Wang, J. Cao, Electrochim. Acta 343 (2020), 136070.
[32] X. Lin, J. Park, L. Liu, Y. Lee, A.M. Sastry, W. Lu, J. Electrochem. Soc. 160 (2013) A1701–A1710.
[33] A. Ghosh, J.M. Foster, G. Offer, M. Marinescu, J. Electrochem. Soc. 168 (2021), 020509.
[34] M. Doyle, T.F. Fuller, J. Newman, J. Electrochem. Soc. 140 (1993) 1526–1533.
[35] T.F. Fuller, M. Doyle, J. Newman, J. Electrochem. Soc. 141 (1994) 1–10.
[36] Z. Chen, D.L. Danilov, L.H.J. Raijmakers, K. Chayambuka, M. Jiang, L. Zhou, J. Zhou, R.-A. Eichel, P.H.L. Notten, J. Power Sources 509 (2021), 230345.
[37] Z. Chen, D.L. Danilov, R.-A. Eichel, P.H.L. Notten, Energy Storage Mater. 48 (2022) 475–486.
[38] Z. Chen, D.L. Danilov, R.-A. Eichel, P.H.L. Notten, Electrochem. Commun. 121 (2020), 106865.
[39] S.-c. Yang, Y. Hua, D. Qiao, Y.-b. Lian, Y.-w. Pan, Y.-l. He, Electrochim. Acta 326 (2019), 134928.
[40] J. Liang, Y. Gan, M. Yao, Y. Li, Int. J. Heat Mass Transf. 165 (2021), 120615.
[41] S. Dhillon, G. Hernández, N.P. Wagner, A.M. Svensson, D. Brandell, Electrochim. Acta 377 (2021), 138067.
[42] Y.-X. Lin, Z. Liu, K. Leung, L.-Q. Chen, P. Lu, Y. Qi, J. Power Sources 309 (2016) 221–230.
[43] D. Li, D.L. Danilov, L. Gao, Y. Yang, P.H.L. Notten, Electrochim. Acta 210 (2016) 445–455.
[44] D. Li, H. Li, D. Danilov, L. Gao, J. Zhou, R.-A. Eichel, Y. Yang, P.H.L. Notten, J. Power Sources 396 (2018) 444–452.
[45] D. Li, D.L. Danilov, B. Zwikirsch, M. Fichtner, Y. Yang, R.-A. Eichel, P.H.L. Notten, J. Power Sources 375 (2018) 106–117.
[46] Y.-T. Cheng, M.W. Verbrugge, J. Power Sources 190 (2009) 453–460.
[47] X. Jin, A. Vora, V. Hoshing, T. Saha, G. Shaver, R.E. García, O. Wasynczuk, S. Varigonda, J. Power Sources 342 (2017) 750–761.
[48] X. Jin, C. Liu, Electrochim. Acta 312 (2019) 188–201.
[49] R. Koerver, W. Zhang, L. de Biasi, S. Schweidler, A.O. Kondrakov, S. Kolling, T. Brezesinski, P. Hartmann, W.G. Zeier, J. Janek, Energy Environ. Sci. 11 (2018) 2142–2158.
[50] L. de Biasi, A.O. Kondrakov, H. Geßwein, T. Brezesinski, P. Hartmann, J. Janek, J. Phys. Chem. C 121 (2017) 26163–26171.
[51] X. Zhang, W. Shyy, A. Marie Sastry, J. Electrochem. Soc. 154 (2007) A910.
[52] W. Ai, L. Kraft, J. Sturm, A. Jossen, B. Wu, J. Electrochem. Soc. 167 (2019), 013512.
[53] Y. Wang, S. Nakamura, M. Ue, P.B. Balbuena, J. Am. Chem. Soc. 123 (2001) 11708–11718.
[54] M. Safari, M. Morcrette, A. Teyssot, C. Delacourt, J. Electrochem. Soc. 156 (2009) A145.
[55] D. Danilov, R.A.H. Niessen, P.H.L. Notten, J. Electrochem. Soc. 158 (2011) A215.
[56] L.H.J. Raijmakers, D.L. Danilov, R.A. Eichel, P.H.L. Notten, Electrochim. Acta 330 (2020), 135147.
[57] S. Pal, S.S. Damle, S.H. Patel, M.K. Datta, P.N. Kumta, S. Maiti, J. Power Sources 246 (2014) 149–159.
[58] P.F. Lory, B. Mathieu, S. Genies, Y. Reynier, A. Boulineau, W. Hong, M. Chandesris, J. Electrochem. Soc. 167 (2020), 120506.
[59] K.P.C. Yao, J.S. Okasinski, K. Kalaga, J.D. Almer, D.P. Abraham, Adv. Energy Mater. 9 (2019), 1803380.
[60] J. Christensen, J. Newman, J. Solid State Electrochem. 10 (2006) 293–319.
[61] L.O. Valøen, J.N. Reimers, J. Electrochem. Soc. 152 (2005) A882–A891.
[62] N. Jin, D.L. Danilov, P.M.J. Van den Hof, M.C.F. Donkers, Int. J. Energy Res. 42 (2018) 2417–2430.
[63] D. Li, H. Li, D.L. Danilov, L. Gao, X. Chen, Z. Zhang, J. Zhou, R.-A. Eichel, Y. Yang, P.H.L. Notten, J. Power Sources 416 (2019) 163–174.
[64] M. Dubarry, C. Truchot, B.Y. Liaw, J. Power Sources 219 (2012) 204–216.
[65] X. Han, M. Ouyang, L. Lu, J. Li, Y. Zheng, Z. Li, J. Power Sources 251 (2014) 38–54.
[66] M. Dubarry, M. Berecibar, A. Devie, D. Anseán, N. Omar, I. Villarreal, J. Power Sources 360 (2017) 59–69.
[67] C. Pastor-Fernández, K. Uddin, G.H. Chouchelamane, W.D. Widanage, J. Marco, J. Power Sources 360 (2017) 301–318.
[68] S. Lee, J.B. Siegel, A.G. Stefanopoulou, J.-W. Lee, T.-K. Lee, J. Electrochem. Soc. 167 (2020), 090531.
[69] D. Anseán, M. Dubarry, A. Devie, B.Y. Liaw, V.M. García, J.C. Viera, M. González, J. Power Sources 356 (2017) 36–46.
[70] B. Pan, D. Dong, J. Wang, J. Nie, S. Liu, Y. Cao, Y. Jiang, Electrochim. Acta 362 (2020), 137101.
[71] P.P. Paul, V. Thampy, C. Cao, H.-G. Steinrück, T.R. Tanim, A.R. Dunlop, E.J. Dufek, S.E. Trask, A.N. Jansen, M.F. Toney, J. Nelson Weker, Energy Environ. Sci. 14 (2021) 4979–4988.
[72] S. Gantenbein, M. Schönleber, M. Weiss, E. Ivers-Tiffée, Sustainability 11 (2019) 6697.
[73] A. Lamorgese, R. Mauri, B. Tellini, J. Energy Storage 20 (2018) 289–297.
[74] A. Sarkar, P. Shrotriya, A. Chandra, C. Hu, J. Energy Storage 25 (2019), 100911.
[75] M.B. Pinson, M.Z. Bazant, J. Electrochem. Soc. 160 (2013) A243–A250.
[76] J. Keil, A. Jossen, J. Electrochem. Soc. 167 (2020), 110535.
[77] L. von Kolzenberg, A. Latz, B. Horstmann, ChemSusChem (2020).
[78] Y. Xu, H. Wu, H. Jia, J.G. Zhang, W. Xu, C. Wang, ACS Nano 14 (2020) 8766–8775.
[79] J.P. Pender, G. Jha, D.H. Youn, J.M. Ziegler, I. Andoni, E.J. Choi, A. Heller, B. S. Dunn, P.S. Weiss, R.M. Penner, C.B. Mullins, ACS Nano 14 (2020) 1243–1295.
[80] M. Haruta, T. Okubo, Y. Masuo, S. Yoshida, A. Tomita, T. Takenaka, T. Doi, M. Inaba, Electrochim. Acta 224 (2017) 186–193.
[81] M. Ecker, J.B. Gerschler, J. Vogel, S. Käbitz, F. Hust, P. Dechent, D.U. Sauer, J. Power Sources 215 (2012) 248–257.
[82] R. Spotnitz, J. Power Sources 113 (2003) 72–80.
[83] Y. Li, Z. Wei, B. Xiong, D.M. Vilathgamuwa, IEEE Trans. Ind. Electron. 69 (2022) 6984–6996.
[84] K. Liu, Z. Wei, C. Zhang, Y. Shang, R. Teodorescu, Q.-L. Han, IEEE/CAA Journal of Automatica Sinica (2022) 1139–1165.
[85] Z. Wei, Z. Quan, J. Wu, Y. Li, J. Pou, H. Zhong, IEEE Trans. Ind. Electron. 69 (2022) 2588–2598.
[86] Z. Khalik, H.J. Bergveld, M.C.F. Donkers, in: 2021 American Control Conference (ACC), New Orleans, USA, 2021.
[87] Z. Khalik, H.J. Bergveld, M.C.F. Donkers, in: 2020 American Control Conference, Denver, USA, 2020.
[88] Z. Chen, D.L. Danilov, R.A. Eichel, P.H.L. Notten, Adv. Energy Mater. 12 (2022) 2201506.